AD-A160 370 THE AFGL GLOBAL SPECTRAL MODEL: EXPANDED RESOLUTION BASELINE VERSION(U) AIR FORCE GEOPHYSICS LAB HANSCOM AFB MA S BRENNER ET AL. 16 NOV 84 AFGL-TR-84-0308 1/1

UNCLASSIFIED F/G 4/2 NL

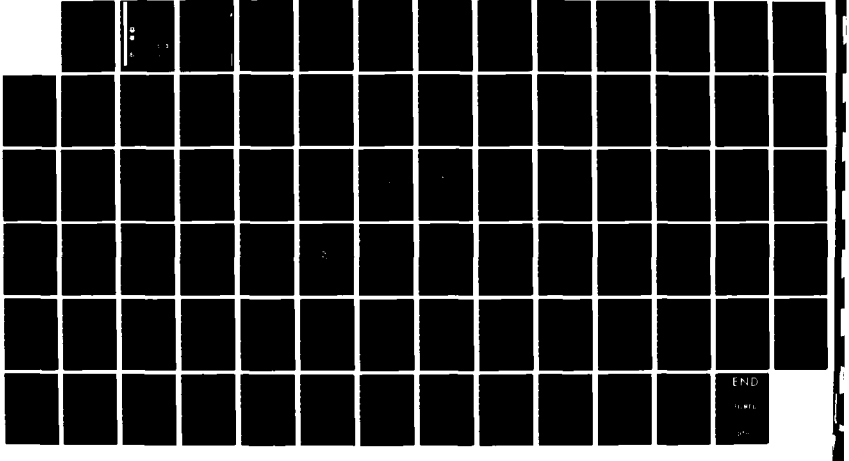

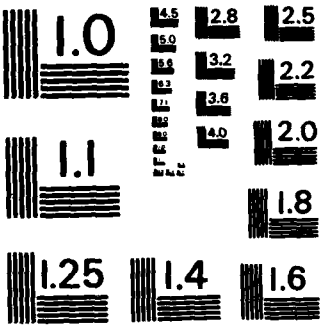

MICROCOPY RESOLUTION TEST CHART
NATIONAL BUREAU OF STANDARDS - 1963 - A

AFGL-TR-84-0308
ENVIRONMENTAL RESEARCH PAPERS, NO. 896

(12)

AD-A160 370

The AFGL Global Spectral Model: Expanded Resolution Baseline Version

STEPHEN BRENNER
CHIEN-HSIUNG YANG
KENNETH MITCHELL

16 November 1984

ATMOSPHERIC SCIENCES DIVISION PROJECT 2310
AIR FORCE GEOPHYSICS LABORATORY
HANSCOM AFB, MA 01731

"This technical report has been reviewed and is approved for publication"

FOR THE COMMANDER

for DONALD A. CHISHOLM, Chief
Atmospheric Prediction Branch

ROBERT A. McCLATCHEY, Director
Atmospheric Sciences Division

This document has been reviewed by the ESD Public Affairs Office (PA) and is releasable to the National Technical Information Service (NTIS).

Qualified requestors may obtain additional copies from the Defense Technical Information Center. All others should apply to the National Technical Information Service.

If your address has changed, or if you wish to be removed from the mailing list, or if the addressee is no longer employed by your organization, please notify AFGL/DAA, Hanscom AFB, MA 01731. This will assist us in maintaining a current mailing list.

Unclassified
SECURITY CLASSIFICATION OF THIS PAGE

AD-A160 370

REPORT DOCUMENTATION PAGE

1a. REPORT SECURITY CLASSIFICATION: Unclassified	1b. RESTRICTIVE MARKINGS
2a. SECURITY CLASSIFICATION AUTHORITY	3. DISTRIBUTION/AVAILABILITY OF REPORT: Approved for public release; distribution unlimited
2b. DECLASSIFICATION/DOWNGRADING SCHEDULE	
4. PERFORMING ORGANIZATION REPORT NUMBER(S): AFGL-TR-84-0308 ERP No. 895	5. MONITORING ORGANIZATION REPORT NUMBER(S)
6a. NAME OF PERFORMING ORGANIZATION: Air Force Geophysics Laboratory; 6b. OFFICE SYMBOL (If applicable): LYP	7a. NAME OF MONITORING ORGANIZATION: /
6c. ADDRESS (City, State and ZIP Code): Hanscom Air Force Base Massachusetts 01731	7b. ADDRESS (City, State and ZIP Code)
8a. NAME OF FUNDING/SPONSORING ORGANIZATION; 8b. OFFICE SYMBOL (If applicable)	9. PROCUREMENT INSTRUMENT IDENTIFICATION NUMBER
8c. ADDRESS (City, State and ZIP Code)	10. SOURCE OF FUNDING NOS.

PROGRAM ELEMENT NO	PROJECT NO	TASK NO.	WORK UNIT NO
62101F	2310	G7	03

11. TITLE (Include Security Classification): The AFGL Global Spectral Model: (Contd)

12. PERSONAL AUTHOR(S): Brenner, Stephen; Yang, Chien-Hsiung; Mitchell, Kenneth

13a. TYPE OF REPORT	13b. TIME COVERED	14. DATE OF REPORT (Yr., Mo., Day)	15. PAGE COUNT
Final	FROM 1/10/82 TO 30/9/84	1984 November 16	80

16. SUPPLEMENTARY NOTATION

17. COSATI CODES		
FIELD	GROUP	SUB. GR.

18. SUBJECT TERMS (Continue on reverse if necessary and identify by block number)
Atmospheric models
Spectral models
Weather forecasting
Numerical weather prediction
Global atmospheric circulation

19. ABSTRACT (Continue on reverse if necessary and identify by block number)

The flexible resolution/truncation baseline version of the AFGL global spectral model as adapted to the CRAY-1 is described. A series of low-resolution (6 layer, rhomboidal 15) and high-resolution (12 layer, rhomboidal 30) forecasts were run and compared to test the performance of the model. In general, higher resolution resulted in improved forecast skill in the 24-to-96-hour range. The only exception to this is the humidity forecast, which shows minimal skill. This characteristic is rather insensitive to the resolution partly because of the poor quality of analyzed humidity fields used for initial data and verification.

The original gridded (2.5° x 2.5°) topography has been replaced by a smoothed terrain field that has been passed through a nine-point smoother, interpolated to the model's Gaussian grid, and then spectrally truncated.

Finally, the effects of initialization have been studied by comparing a series of forecasts subjected to several initialization methods. For forecasts beyond (Contd)

20. DISTRIBUTION/AVAILABILITY OF ABSTRACT	21. ABSTRACT SECURITY CLASSIFICATION
UNCLASSIFIED/UNLIMITED ☒ SAME AS RPT ☐ DTIC USERS ☐	Unclassified

22a. NAME OF RESPONSIBLE INDIVIDUAL	22b. TELEPHONE NUMBER (Include Area Code)	22c. OFFICE SYMBOL
Stephen Brenner	(617) 861-2962	LYP

DD FORM 1473, 83 APR EDITION OF 1 JAN 73 IS OBSOLETE

Unclassified
SECURITY CLASSIFICATION OF THIS PAGE

Block 11 (Contd):

Expanded Resolution Baseline Version

Block 19 (Contd):

24 hours, the model is able to supress spurious gravity waves through the combined effects of the semi-implicit time scheme and the subgrid scale diffusion. The impact of normal mode initialization is seen mainly in the very short-range forecasts (less than 24 hours) and is thus important for providing smooth first-guess fields for the analysis/data assimilation cycle.

Contents

Illustrations

Tables

Tables

The AFGL Global Spectral Model: Expanded Resolution Baseline Version

1. INTRODUCTION

This report is the second in a series that will serve as the documentation of the AFGL global spectral model. The progress reported here deals primarily with (1) the changes necessary to expand the resolution of the baseline model[1] and adapt it to the CRAY-1 computer, and (2) evaluation of the high-resolution (30R12) model. The term "baseline version" version refers to the mathematical/numerical formulation and model configuration as described by Brenner et al[1] (hereafter referred to as TR-1). The reader is referred to that report for the appropriate details.

2. EXPANDED RESOLUTION BASELINE MODEL

As mentioned in section 1, the expanded resolution version of the AFGL global model is an extension of the baseline version described in TR-1. Briefly, the model is a global spectral model using spherical harmonics to represent horizontal variations and discrete layers with the Arakawa differencing scheme to represent vertical variations. Nonlinear terms in the tendencies of vorticity, divergence,

(Received for publication 15 November 1984)

1. Brenner, S., Yang, C., and Yee, S. (1982) The AFGL Spectral Model of the Moist Global Atmosphere: Documentation of the Baseline Version, AFGL-TR-82-0393, AD A129283.

temperature, moisture, and surface pressure are computed using the transform method.[2,3] Time differencing is performed with the semi-implicit scheme. The independent variables of the model are time, t; longitude and latitude, λ and ϕ; and the terrain following vertical coordinate, $\sigma = p/p_*$. Dependent variables of the model include:

(1) prognostic variables

η absolute vorticity

D divergence

T temperature

q natural log of surface pressure

Q specific humidity

(2) diagnostic variables

Φ geopotential

$\dot{\sigma}$ vertical velocity

U, V horizontal pseudo-velocity components

For completeness, the continuous model equations are given here: the vorticity and divergence equations,

$$\frac{\partial \eta}{\partial t} = -\frac{1}{a\cos^2\phi}\left[\frac{\partial A}{\partial \lambda} + \cos\phi \frac{\partial B}{\partial \phi}\right] + \underset{\sim}{k}\cdot\nabla \times \underset{\sim}{F}_h \tag{1}$$

$$\frac{\partial D}{\partial t} = \frac{1}{a\cos^2\phi}\left[\frac{\partial B}{\partial \lambda} - \cos\phi \frac{\partial A}{\partial \phi}\right] - \nabla^2\left[E + \Phi + RT_0 q\right] + \nabla\cdot\underset{\sim}{F}_h; \tag{2}$$

the thermodynamic equation,

$$\frac{\partial T}{\partial t} = -\frac{1}{a\cos^2\phi}\left[\frac{\partial UT'}{\partial \lambda} + \cos\phi \frac{\partial VT'}{\partial \phi}\right] + T'D$$

$$-\sigma^{\kappa}\dot{\sigma}\frac{\partial T\sigma^{\kappa}}{\partial \sigma} + \frac{RT}{C_p}\left[C - \overline{C} - \overline{D}\right] + \frac{H}{C_p} + {}_hF_T; \tag{3}$$

---

2. Eliasen, E., Machenauer, B., and Rasmussen, E. (1970) On a Numerical Method for Integration of the Hydrodynamical Equations With a Spectral Representation of the Horizontal Fields, Inst. of Theoret. Meteor., U. of Copenhagen, Report No. 2.

3. Orszag, S.A. (1970) Transform method for calculation of vector coupled sums: Application to the spectral form of the vorticity equation, J. Atmos. Sci. 27:890-895.

the moisture equation,

$$\frac{\partial Q}{\partial t} = - \frac{1}{a \cos^2\phi}\left[\frac{\partial UQ}{\partial \lambda} + \cos\phi \frac{\partial VQ}{\partial \phi}\right] + QD - \dot{\sigma} \frac{\partial Q}{\partial \sigma} + S + {}_hF_Q; \tag{4}$$

the continuity equation,

$$\frac{\partial q}{\partial t} = - \overline{C} - \overline{D}; \tag{5}$$

the hydrostatic equation,

$$\frac{\partial \Phi}{\partial \sigma^\kappa} = - C_p T \sigma^{-\kappa}; \tag{6}$$

and diagnostic equations for the velocity components,

$$\dot{\sigma} = \sigma(\overline{C} + \overline{D}) - \overset{-\sigma}{C} - \overset{-\sigma}{D} \tag{7}$$

$$U = - \frac{\cos\phi}{a} \frac{\partial \psi}{\partial \phi} + \frac{1}{a} \frac{\partial \chi}{\partial \lambda} \tag{8}$$

$$V = \frac{1}{a} \frac{\partial \psi}{\partial \lambda} + \frac{\cos\phi}{a} \frac{\partial \chi}{\partial \phi} \tag{9}$$

$$\zeta = \nabla^2 \psi \tag{10}$$

$$D = \nabla^2 \chi \tag{11}$$

where

$$A = \eta U + \dot{\sigma} \frac{\partial V}{\partial \sigma} + \frac{RT'}{a} \cos\phi \frac{\partial q}{\partial \phi} + \frac{g}{p_*} \frac{\partial \tau_\phi}{\partial \sigma} \tag{12}$$

$$B = \eta V - \dot{\sigma} \frac{\partial U}{\partial \sigma} - \frac{RT'}{a} \frac{\partial q}{\partial \lambda} - \frac{g}{p_*} \frac{\partial \tau_\lambda}{\partial \sigma} \tag{13}$$

$$E = \frac{U^2 + V^2}{2 \cos^2\phi}, \tag{14}$$

$$q = \ln p_* \tag{15}$$

$$C = \underset{\sim}{v} \cdot \nabla q, \tag{16}$$

$$\overset{-\sigma}{(\,)} = \int_0^{\sigma} (\,)\, d\sigma \text{ and } \overline{(\,)} = \int_0^1 (\,)\, d\sigma, \tag{17}$$

F_h is the parameterized subgrid-scale horizontal diffusion, and T' is the deviation of temperature from the reference value $T_o(\sigma)$.

Parameterized physical processes in the model include the following: a bulk aerodynamic boundary layer formulation, large-scale condensation, Kuo-type moist convection, dry convective adjustment, and subgrid scale diffusion. Once again, the reader is referred to TR-1 for the details of these aspects of the model.

3. FLEXIBLE RESOLUTION/TRUNCATION

The baseline version of the AFGL global spectral model was originally coded for the CDC-6600 with a user available central memory of approximately 98 kilowords (K-words). To keep the model core contained, it was configured with six layers and rhomboidal truncation at wavenumber 15, thus requiring 85 K-words for execution.

At the time, we realized that the baseline version was only a preliminary step in the construction of the model. For future research, especially in the area of cloud forecasting, a higher resolution model would be needed, one that was at least comparable to the current operational spectral model at the National Meteorological Center (NMC)[4] (that is, 12 layers and rhomboidal truncation at wavenumber 30).

To construct the high-resolution model, the obvious procedure would have been to replace all of the resolution-dependent parameters (for example, array dimensions and loop limits) with appropriate high-resolution values. However, this again would limit the model to a particular resolution. Thus, to make the model as flexible as possible, following the approach of Sela, [4] the resolution-dependent parameters were replaced with dummy non-Fortran symbols that could be easily changed to any values using a text editor or some type of Fortran preprocessor. The same technique was also applied to the data preprocessing, forecast postprocessing, and normal mode initialization codes.

In coding the model, two additional aspects of flexibility were also considered,

---

4. Sela, J. (1980) Spectral modeling at the National Meteorological Center, Mon. Wea. Rev. 108:1279-1292.

modular structure and portability of the code. In the area of modularity, as much as possible, the code was structured into subroutines corresponding to various mathematical and physical aspects of the model. This allows for easy replacement of various components of the model with new algorithms. This flexibility is crucial, especially in the parts of the model that handle the physical parameterizations that will be replaced with new formulations. To keep the model as portable as possible, all machine-dependent structures and subroutine calls were replaced by standard Fortran equivalents. As a result of this effort, the model, with very minor modifications, has run successfully on the following computers: CDC-6600, CDC-6400, CYBER-750, CRAY-1, Harris-800, and FPS-1 array processor attached to a VAX 11/780.

In addition to flexible resolution, the model can be run with a choice of rhomboidal or triangular truncation. For rhomboidal truncation, the spectral expansions are of the form

$$f(\lambda, \phi, \sigma, t) = \sum_{m=-M}^{M} \sum_{n=|m|}^{|m|+M} f_n^m (\sigma, t) P_n^m (\sin\phi) e^{im\lambda} \tag{18}$$

with $(2M + 1)(M + 1)$ spectral degrees of freedom, and P_n^m is the associated Legendre function of order m and degree n. The transform grid consists of at least $3M + 1$ equally spaced longitudes and at least $(5M + 1)/2$ Gaussian latitudes. For triangular truncation, the expansions are of the form

$$f(\lambda, \phi, \sigma, t) = \sum_{m=-M}^{M} \sum_{n=|m|}^{M} f_n^m (\sigma, t) P_n^m (\sin\phi) e^{im\lambda} \tag{19}$$

with $(M + 1)^2$ degrees of freedom, and a transform grid of at least $3M + 1$ equally spaced longitudes and at least $(3M + 1)/2$ Gaussian latitudes.

Figure 1 shows the spectral domain for the low- and high-resolution versions of the model. The low-resolution versions are rhomboidal 15 (indicated as 15R) and triangular 21 (21T) with 496 or 484 degrees of freedom respectively. The high-resolution versions are 30R and 42T with 1891 and 1849 degrees of freedom respectively.

For efficiency and convenience, the rhomboidal and triangular versions are maintained as separate codes. The reason for this is related to the method of storage of the spectral coefficients. For rhomboidal truncation, the spectral domain (Figure 1) can be easily mapped into a square array as shown in Figure 2a. Each coefficient is referred to by two indices (mm, nj) which are related to the mathematical indices (m, n) by

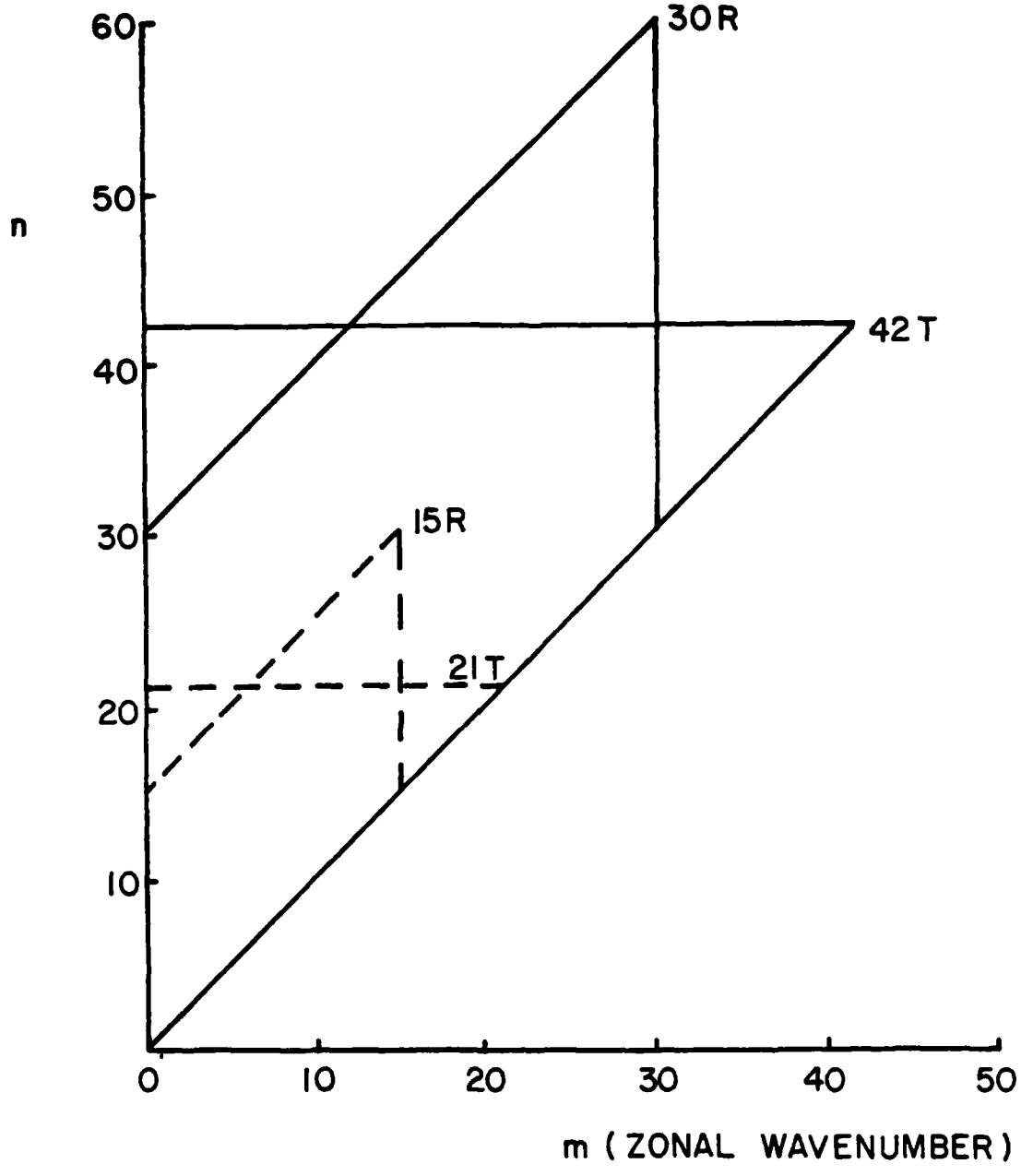

Figure 1. Spectral Domain Showing Low and High Resolutions, Rhomboidal and Triangular Truncations

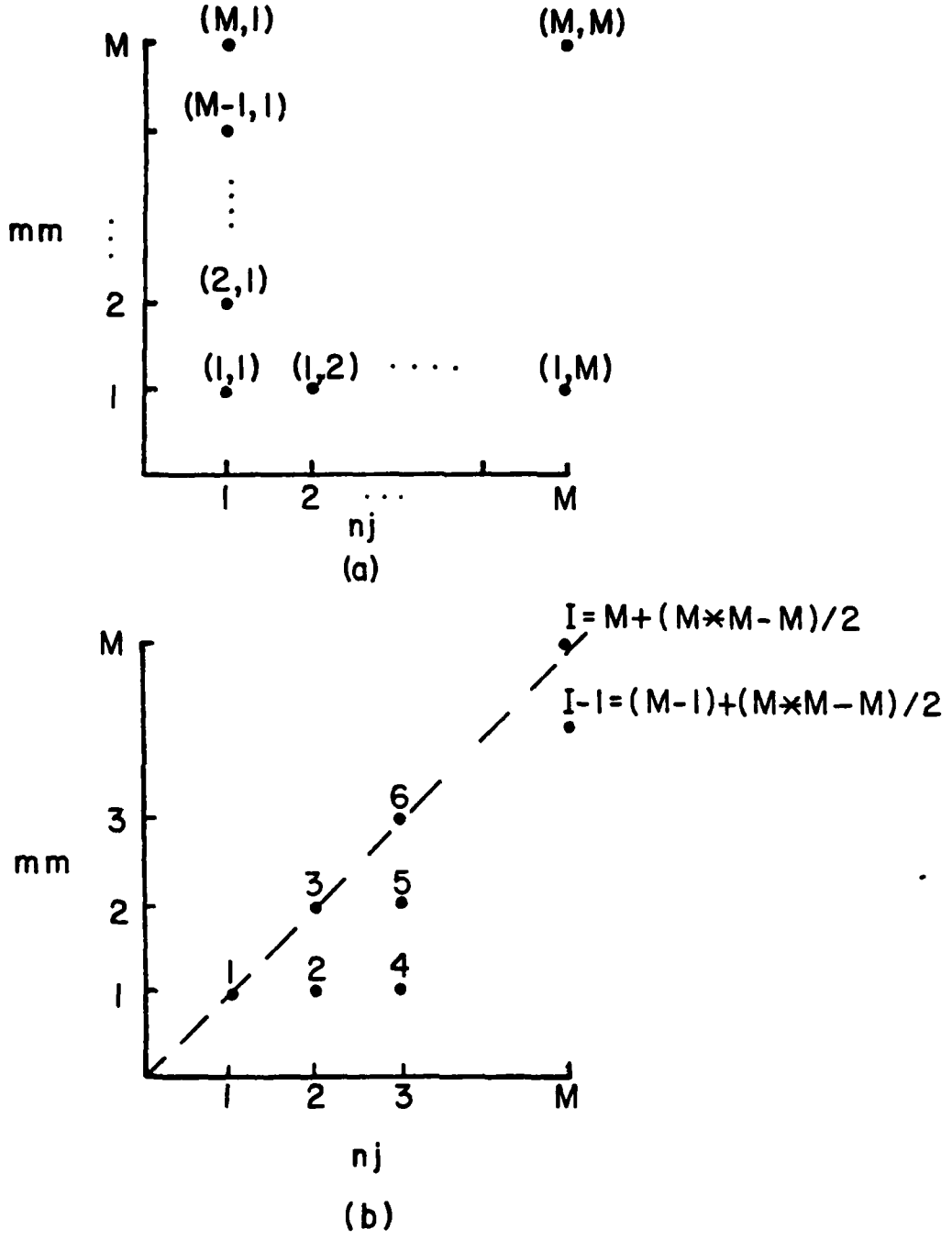

Figure 2. Arrays for Storing Spectral Coefficients: (a) Rhomboidal Truncation, and (b) Triangular Truncation

$$m = mm - 1 \tag{20}$$

$$n = nj + mm - 2. \tag{21}$$

The triangular truncation could also be handled in this manner. However, it would be rather inefficient, since almost half of the array elements would be zero. Instead, the coefficients are stored by columns in a one-dimensional array (Figure 2b). Each coefficient is now referred to by a single index ix obtained from the relationships

$$ix = mm + (nj * nj - nj)/2 \tag{22}$$

$$m = mm - 1 \tag{23}$$

$$n = nj - 1 \tag{24}$$

where (mm, nj) are the corresponding square array indices and (m, n) are the mathematical indices.

As might be expected, an increase in model resolution results in an increase of execution time and core usage. Table 1 gives the computational requirements on the CRAY-1 for various resolutions of the moist model. The resolution is indicated as mRk or mTk where m is the truncation wavenumber, R or T refers to the type of truncation (rhomboidal or triangular), and k is the number of layers in the vertical.

A comparison of 15R12 and 21T12 indicates that, for roughly the same number of degrees of freedom, the triangular version runs somewhat slower. Two reasons exist for this. First, the 21T12 performs more computations because of a larger transform grid of 64 x 34 (2176 points) as compared to 48 x 40 (1920 points) for 15R12. The second reason, elaborated upon in section 4, is that vectorization is not as efficient for triangular truncation.

4. VECTORIZATION

The first step in transferring the model to the CRAY-1 consisted of removing all machine dependent structures (for example, multiple statements on a single line) and replacing all calls to machine language routines by standard Fortran equivalents. Thus, with relatively little effort, a running version of the model was put on the CRAY-1. This will be referred to as "the original version of the model." From the first three lines of Table 2, it can be seen that the original

Table 1. Computational Requirements on the CRAY-1 for Various Resolutions of the Moist Model

Model (resolution)	cpu time (sec)/model time step	core (K-words)
15R6	1.10	89
15R12	2.02	137
21T12	2.59	145
30R12	9.72	393
42T12	13.68	408

version of the model ran 12-13 times faster on the CRAY-1 than on the CDC-6600 with maximum compiler optimization. However, the small difference between the scalar and vector execution times on the CRAY-1 (lines 2 and 3 in Table 2) indicates that the original code was not structured properly for vectorization.

Table 2. Effects of Restructuring Code (Vectorization) on Execution Time for a 24-Hour Moist Forecast Using Six Layers and Rhomboidal M = 15

Model Version / hardware (compiler)		cpu time (sec)
original / CDC-6600	(opt = 2)	1076
original / CRAY-1	(scalar)	89
original / CRAY-1	(vector)	82
vectorized / CDC-6600	(opt = 2)	679
vectorized / CYBER-750	(opt = 2)	225
vectorized / CRAY-1	(scalar)	49
vectorized / CRAY-1	(vector)	27

To take advantage of the vector processing capabilities of the CRAY-1, we tried to rewrite the model in a more efficient form. We focused primarily on those subroutines that handle the transforms, since they comprise the most time-consuming portion of the code. The code resulting from this restructuring will be referred to as "the vectorized version." Table 2 shows that the vectorized version of the model runs more efficiently than the original on both the CDC-6600 and the CRAY-1. The net effect of restructuring the code (comparing lines 3 and 7) is a speed-up by a factor of three. A comparison of the original version on the CDC-6600 with the vectorized version on the CRAY-1 (lines 1 and 7) shows an overall speed-up of a factor of 40.

Finally, Table 1 compares the relative efficiencies of the two different truncations. For a comparable number of spectral degrees of freedom (15R12 compared to 21T12), Table 1 shows that the triangular truncation required 28% more execution time. As was mentioned in Section 3, there are two reasons for this, each accounting for roughly half of the additional time. First, the triangular version has a slightly larger transform grid and thus performs more grid point calculations. The second reason is that the triangular version is not as amenable to vectorization because of the structure of the computational vectors used in the Legendre transform and Gaussian quadrature. The difference is that the rhomboidal vectors are all of a fixed length, while the triangular vectors are of varying lengths and thus not as amenable to efficient vector processing. However, methods exist to further optimize the triangular code and reduce the gap between the two truncations. Some of these methods will be examined in the near future.

5. REVISED PREPROCESSING AND POSTPROCESSING

As in TR-1 the 1978 FGGE level III-A data are still being used as the input and verifying data. The terms "preprocessing" and "postprocessing" were introduced in TR-1 to describe the procedures required for the transformations before and after prognostication, respectively, between the analysis (or data) grid and the model grid.

Two revisions have been made to the procedures described in TR-1. The first is that instead of the analyzed temperature from the FGGE data, a new set of temperature values on the mandatory levels is now used to calculate the initial values of temperature and geopotential in the model grid. These new values are obtained by solving a linear system of equations that accord with the least-squares principle and that use the analyzed height data as the input. The new set of temperature values is closer to being in hydrostatic balance with the set of analyzed height values than is the set of analyzed temperature values and is, therefore, more suitable for input to the model.

The second revision is in the vertical interpolation of humidity. Previously, values of relative humidity on mandatory pressure levels in the FGGE data set were converted into specific humidity prior to the vertical interpolation step where it is assumed that the chosen humidity variable varies linearly with the logarithm of pressure between any two consecutive data levels. A study by Mitchell and Yang,[5] however, demonstrated convincingly that specific humidity

5. Mitchell, K., and Yang, C. (1984) A Comparison of Moisture Variables in the Vertical Interpolation of a 4-D Data Assimilation System, AFGL Technical Report in preparation.

does not vary linearly with the logarithm of pressure. Thus, in conjunction with the interpolation and extrapolation procedures currently used, relative humidity is more suitable as the variable of interpolation. Accordingly, the conversion from relative humidity to specific humidity in the preprocessing has been shifted to follow the vertical interpolation. Similarly, in the postprocessing, the conversion from specific humidity to relative humidity is now done before the vertical interpolation.

In the comparison of different resolutions reported in sections 6, 7 and 8, the same assumptions and algorithms have been used to perform both preprocessing and postprocessing regardless of resolution, since the main objective of the study is to assess the influence of resolution on model forecasts. In the vertical interpolations between the analysis and model grids, temperature, wind, and relative humidity are all assumed to vary linearly with the logarithm of pressure in the layer bounded by any two consecutive levels where data are available.

Since the model treats the atmosphere as a number of discrete layers, a representative pressure level must be defined for each layer. The prognostic variables at these levels are determined by interpolating from the analyzed values at the adjacent mandatory pressure levels. It should be noted that the three phases of the model (preprocessing, forecasting, and postprocessing) do not agree with each other in assigning layer temperatures to pressure levels.

A layer temperature, $\overline{T}_{k,\,k+1}$, representing the layer bounded by pressures $\tilde{p}_k$ and $\tilde{p}_{k+1}$ that are at heights $\tilde{Z}_k$ and $\tilde{Z}_{k+1}$, respectively, is defined as

$$\overline{T}_{k,\,k+1} = \frac{g}{R} \frac{\tilde{Z}_k - \tilde{Z}_{k+1}}{\ln \frac{\tilde{p}_{k+1}}{\tilde{p}_k}} . \tag{25}$$

In the preprocessing phase, this temperature is assigned to a level with pressure $\overline{p}'_{k,\,k+1}$ given by

$$\ln \overline{p}'_{k,\,k+1} = 1/2\,(\ln \tilde{p}_k + \tilde{p}_{k+1}) . \tag{26}$$

In the forecast phase, the temperature in the layer bounded by two sigma interfaces $\tilde{\sigma}_k$, $\tilde{\sigma}_{k+1}$ is assigned to the level with pressure

$$p''_{k,\,k+1} = p_* \left[\frac{1}{1+\kappa} \frac{\tilde{\sigma}_{k+1}^{1+\kappa} - \tilde{\sigma}_k^{1+\kappa}}{\tilde{\sigma}_{k+1} - \tilde{\sigma}_k} \right]^{1/\kappa} \tag{27}$$

where p_* is the surface pressure. Finally, in the postprocessing phase, the same layer temperature is assigned to the level with pressure

$$\bar{p}''_{k,\,k+1} = p_* \left[\frac{\tilde{\sigma}_{k+1}^{\kappa} - \tilde{\sigma}_k^{\kappa}}{\kappa(\ln \tilde{\sigma}_{k+1} - \ln \tilde{\sigma}_k)} \right]^{1/\kappa} \tag{28}$$

Table 3 exhibits the numerical differences among these three pressures in the high-resolution model where the 12-layer structure of the NMC operational model is used.

6. MODEL PERFORMANCE - COMPARISON OF HIGH- AND LOW-RESOLUTION FORECASTS

In the studies reported in the following sections, "low resolution" refers to the forecast model with rhomboidal truncation at wavenumber 15 in the horizontal and 6 layers in the vertical (15R6); "high resolution" refers to the forecast model with rhomboidal truncation at wavenumber 30 in the horizontal and 12 layers in the vertical (30R12). The σ structures are summarized in Table 4. A detailed comparison of the high-resolution rhomboidal (30R) and triangular (42T) will be conducted after the triangular code is further optimized.

Tables 5 and 6 present the statistics of the 24- and 48-hour forecast performances over periods of five consecutive days each in January (15-19 January 1978) and July (16-20 July 1978). Each entry contains the sample mean and the sample standard deviation (in parenthesis) of the global root-mean-square (rms) differences (see TR-1 for details). The standard deviation measures the representativeness of the corresponding mean. Symbols A, F, S, and P stand for analysis, forecast, synthesis, and persistence, respectively. The analysis refers to the fields obtained by interpolating FGGE III-A data from the 2.5° -interval latitude-longitude grid to a 2.5 longitude Gaussian latitude grid. These fields are used both as the input and for verification. The forecast includes preprocessing at the initial time, initialization, prediction, and postprocessing at the verifying time, while the synthesis subjects the FGGE data at the verifying time to the preprocessing and postprocessing. The difference between the synthesis and the analysis is therefore a measure of the direct impact of the interpolations and truncations in

Table 3. Pressure Values (mb) of Levels to Which Layer Temperatures Are Assigned When the NMC 12-Layer Sigma Structure Is Used. In Eqs. (26) and (28), the upper boundary is placed at p = 10 mb (p_* = 1013.25 mb)

k	$\tilde{\sigma}$	$\tilde{p}$	Eq. (26) preprocessing	Eq. (27) forecasting	Eq. (28) postprocessing
	0.	0.			
1			22.51	21.02	23.22
	.050	50.66			
2			71.65	74.97	72.06
	.100	101.33			
3			124.10	126.05	124.34
	.150	151.99			
4			175.50	176.89	175.67
	.200	202.65			
5			226.57	227.65	226.70
	.250	253.31			
6			277.49	278.37	277.60
	.300	303.98			
7			339.85	341.47	340.06
	.375	379.97			
8			438.75	442.22	439.18
	.500	506.63			
9			877.64	581.43	578.11
	.650	658.61			
10			730.66	733.67	731.04
	.800	810.60			
11			871.63	873.38	871.85
	.925	937.26			
12			974.51	975.08	974.58
	1.	1013.25			

Table 4. The σ-Structures

LOW RESOLUTION				HIGH RESOLUTION			
k Index	Δ Thickness	$\tilde{\sigma}$ Interface	σ Layer	k Index	Δ Thickness	$\tilde{\sigma}$ Interface	σ Layer
		0.				0.	
				1	.050		.020747
						.050	
1	.150		.062240	2	.050		.073986
						.100	
				3	.050		.124400
		.150				.150	
				4	.050		.174573
2	.200		.198494			.200	
				5	.050		.224668
		.250				.250	
				6	.050		.274729
						.300	
3	.250		.369929	7	.075		.337003
						.375	
				8	.125		.436433
		.500				.500	
4	.250		.622000	9	.150		.573831
						.650	
		.750		10	.150		.724074
5	.150		.824187			.800	
		.900		11	.125		.961960
6	.100		.949686			.925	
				12	.075		.962326
		1.000				1.000	

Table 5. Performance (Global RMS Difference and Standard Deviations) January 1978. L = low resolution, and H = high resolution

Level (mb)	Pair	Res	V (ms^{-1})		T (°K)		Z (m)		RH (%)	
			24h	48h	24h	48h	24h	48h	24h	48h
850	(F, A)	L	5.28 (.11)	7.08 (.31)	2.60 (.20)	3.64 (.11)	31.56 (.55)	44.38 (1.71)	17.96 (1.05)	21.82 (.41)
		H	5.20 (.14)	6.54 (.19)	2.62 (.16)	3.34 (.15)	27.06 (1.70)	37.64 (2.74)	16.76 (.45)	21.22 (.53)
	(S, A)	L	2.68 (.04)	2.72 (.11)	1.02 (.08)	1.00 (.07)	9.68 (.62)	9.78 (.66)	11.94 (.58)	11.82 (.67)
		H	1.02 (.08)	.98 (.08)	.42 (.04)	.42 (.04)	3.70 (.19)	3.64 (.20)	3.94 (.19)	4.02 (.20)
	(P, A)	L/H	6.92 (.31)	7.70 (.60)	2.88 (.22)	3.52 (.29)	39.04 (1.71)	51.12 (3.59)	10.90 (.64)	12.50 (.94)
500	(F, A)	L	6.98 (.16)	9.62 (.50)	2.02 (.13)	2.76 (.09)	39.86 (1.84)	59.66 (3.83)	23.00 (1.02)	26.98 (.44)
		H	6.40 (.19)	8.32 (.29)	2.74 (.09)	2.42 (.08)	33.14 (2.30)	48.50 (3.04)	20.26 (.75)	26.36 (.58)
	(S, A)	L	3.96 (.11)	4.00 (.07)	1.30 (.10)	1.34 (.13)	13.16 (.74)	12.04 (.76)	15.76 (.78)	15.72 (.76)
		H	1.00 (.12)	.96 (.05)	.38 (.04)	.38 (.04)	4.12 (.13)	4.10 (.14)	5.00 (.16)	5.02 (.15)
	(P, A)	L/H	11.22 (.41)	12.62 (.95)	2.80 (.12)	3.38 (.19)	58.02 (4.74)	73.80 (7.91)	22.22 (.43)	25.64 (.67)
250*	(F, A)	L	11.68 (.25)	14.76 (.38)	4.66 (.09)	5.10 (.07)	55.28 (3.05)	85.86 (4.06)	25.56 (.81)	30.78 (.34)
		H	10.28 (.28)	12.80 (.46)	2.02 (.08)	2.44 (.11)	48.92 (3.32)	72.54 (2.61)	25.00 (.71)	29.96 (.63)
	(S, A)	L	5.94 (.17)	5.96 (.15)	3.08 (.11)	3.08 (.11)	14.64 (.52)	14.52 (.57)	14.90 (.62)	16.00 (.58)
		H	1.34 (.11)	1.32 (.13)	.42 (.04)	.44 (.05)	3.36 (.22)	3.43 (.22)	3.32 (.30)	3.50 (.14)
	(F, A)	L/H	16.92 (.42)	19.06 (1.38)	2.62 (.08)	3.06 (.19)	81.92 (5.49)	101.40 (11.17)	21.34 (.40)	24.64 (.68)

*Relative humidity is at the 300-mb level

Table 6. Performance (Global RMS Differences and Standard Deviations) July 1978. L = low resolution, and H = high resolution

Level (mb)	Pair	Res	V (ms^{-1})		T (°K)		Z (m)		RH (%)	
			24h	48h	24h	48h	24h	48h	24h	48h
850	(F, A)	L	5.02	6.54	2.18	2.98	26.48	38.94	15.96	20.62
			(.23)	(.29)	(.04)	(.07)	(1.88)	(2.35)	(.63)	(.31)
		H	5.10	6.54	2.20	3.06	24.50	37.90	15.46	20.36
			(.26)	(.22)	(.07)	(.19)	(1.63)	(1.11)	(.38)	(.43)
	(S, A)	L	2.44	2.42	0.92	0.96	8.84	8.64	9.20	9.16
			(.09)	(.11)	(.08)	(.11)	(.48)	(.32)	(.24)	(.31)
		H	0.70	0.72	0.40	0.40	3.92	3.84	3.44	3.38
			(.07)	(.04)	(.12)	(.12)	(.29)	(.15)	(.27)	(.31)
	(P, A)	L/H	5.48	7.08	2.14	2.82	29.02	44.08	9.64	11.90
			(.16)	(.16)	(.05)	(.08)	(1.42)	(2.09)	(.30)	(.37)
500	(F, A)	L	6.34	8.36	1.92	2.48	35.90	52.04	22.08	26.12
			(.30)	(.43)	(.04)	(.08)	(2.37)	(3.77)	(.58)	(.62)
		H	6.12	8.22	1.74	2.44	32.62	48.98	19.74	25.40
			(.37)	(.38)	(.09)	(.19)	(2.41)	(2.20)	(.71)	(.78)
	(S, A)	L	3.40	3.40	1.22	1.20	18.64	10.36	15.08	15.20
			(.16)	(.16)	(.11)	(.12)	(.51)	(.51)	(.54)	(.39)
		H	0.74	0.74	0.36	0.34	3.72	3.68	5.34	5.38
			(.05)	(.05)	(.05)	(.05)	(.08)	(.08)	(.23)	(.22)
	(P, A)	L/H	8.14	10.42	2.10	2.86	40.30	59.76	21.10	24.52
			(.30)	(.29)	(.07)	(.09)	(3.34)	(3.31)	(.69)	(.45)
250*	(F, A)	L	11.32	14.12	4.80	5.16	54.46	79.26	26.00	30.06
			(.31)	(.63)	(.10)	(.11)	(1.87)	(3.08)	(.57)	(.95)
		H	9.90	12.50	2.12	2.56	49.56	72.28	26.14	29.78
			(.16)	(.39)	(.08)	(.11)	(3.19)	(3.75)	(.49)	(.45)
	(S, A)	L	6.32	6.30	3.42	3.42	15.36	15.22	15.20	15.20
			(.24)	(.26)	(.04)	(.04)	(.96)	(.93)	(.23)	(.23)
		H	1.32	1.38	0.50	0.52	3.28	3.20	4.84	4.76
			(.22)	(.18)	(.07)	(.04)	(.31)	(.25)	(.30)	(.23)
	(P, A)	L/H	13.00	16.32	2.34	2.68	61.66	89.92	20.62	23.74
			(.82)	(.78)	(.15)	(.13)	(5.57)	(5.77)	(.61)	(.42)

*Relative humidity is at the 300-mb level

the transformations between the data and model grids. Persistence evaluates the difference of analyses between the initial and verifying times (Figure 3).

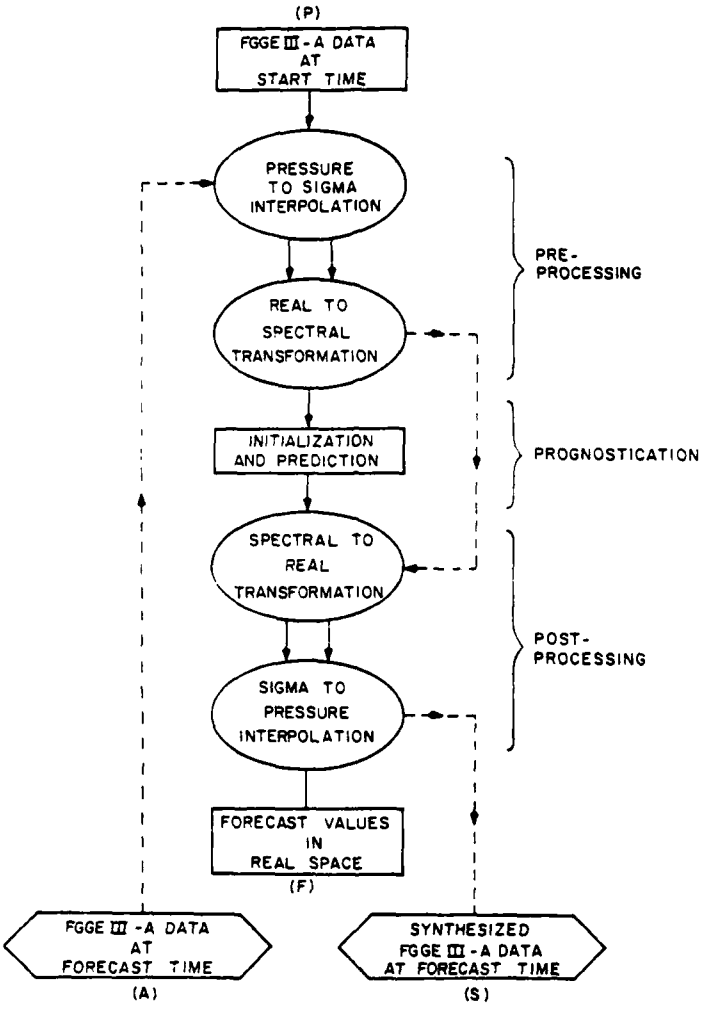

Figure 3. Schematic Diagram of Model Evaluation

The most outstanding difference between the two resolutions appears in the processing errors represented by the difference (S, A). The improved accuracy of the high resolution is found in all variables and at all levels. The magnitudes of the processing errors and the differences due to resolution are similar in the January and July samples. When resolutions were varied both horizontally and vertically, it became clear that most of these improvements resulted from the

horizontal resolution. Figure 4, a meridional cross-section of the rms differences between the synthesized and analyzed 500 mb heights, shows such an example. The only exception to this rule was found in the temperature at the 250 mb level which was affected more by the vertical resolution, as shown in Figure 5.

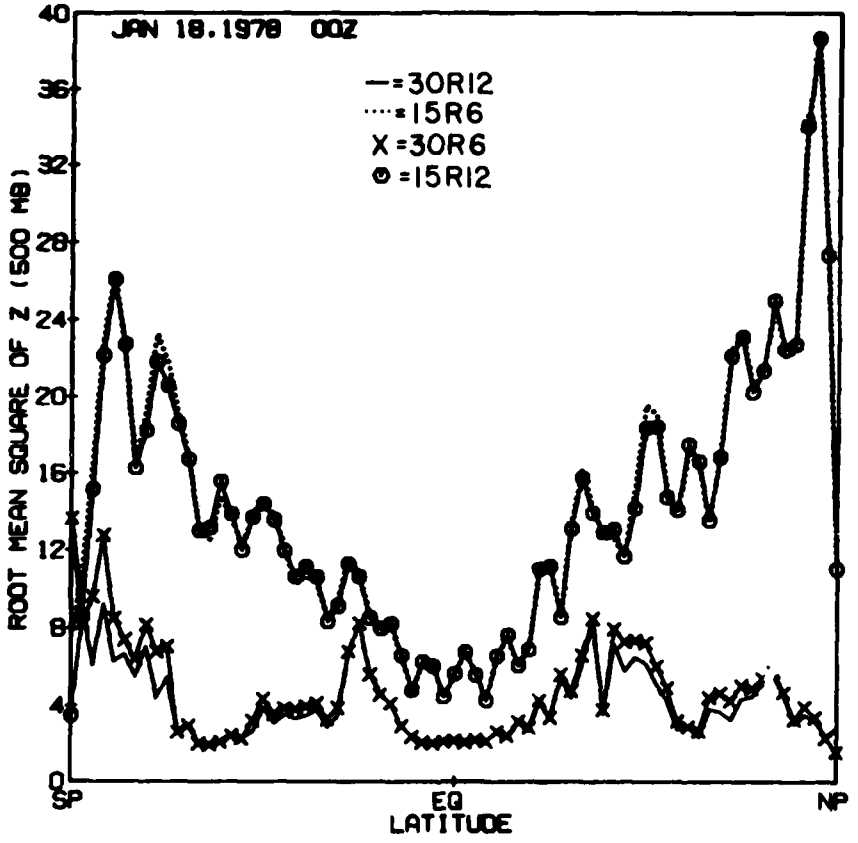

Figure 4. Meridional Profile of Processing Error - RMS Error of 500 mb Heights for Various Resolutions (All Rhomboidal Truncation) for FGGE Data of 00Z 18 January 1978

The main improvements in the forecasts, on the other hand, are found in the heights at all three levels and in the temperature at the 250 mb level. In the latter case, almost all of the improvement in the forecasts appears to result from the reduction in the processing errors produced by the increased vertical resolution. In the improved height forecasts, it is difficult to determine whether the reduction in error is due to the reduced initial error or to the reduced error growth rate.

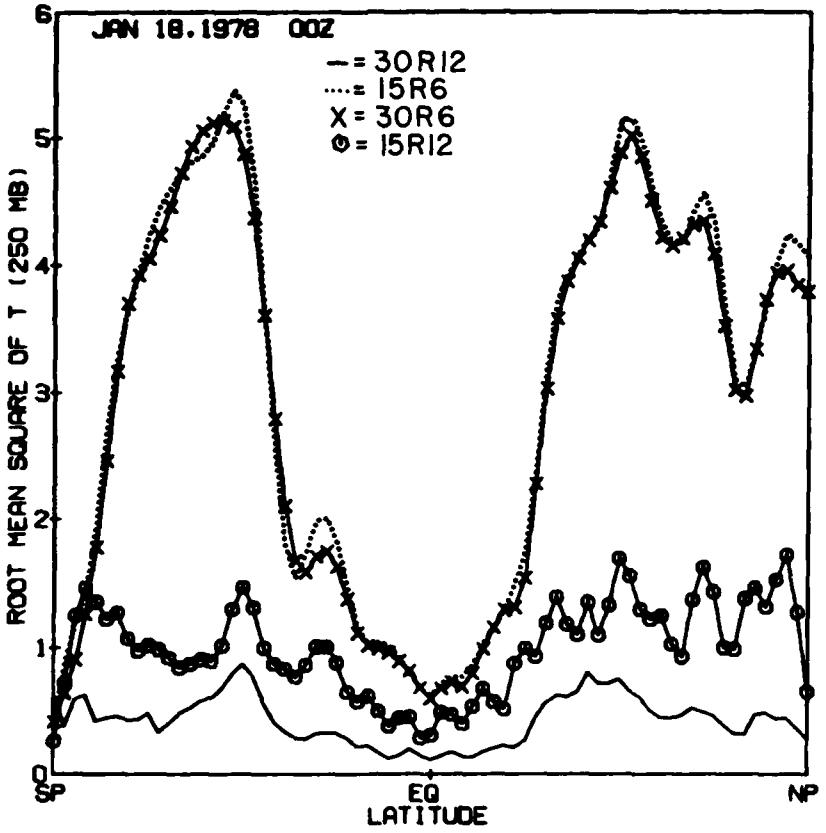

Figure 5. Meridonial Profile of Processing Error - RMS Error of 250 mb Temperatures for Various Resolutions (All Rhomboidal Truncation) for FGGE Data of 00Z 18 January 1978

We will try to answer this question in the future by running and comparing additional resolution experiments. One additional striking feature of the forecast errors is that the relative humidity forecasts are less skillful than persistence. Some of the possible reasons for this will be discussed below.

Figures 6 and 7 summarize some of the more important aspects of the performances and relative skills of the high- and low-resolution models. Figure 6 shows the growth rate of the global rms error of height for the troposphere (average for 1000 to 200 mb) for six forecasts (three in January and three in July). Persistence errors approach the climatic variance (typical value of about 100 m)[6]

---

6. Bengstsson, L. (1981) Numerical prediction of atmospheric blocking: A case Study, Tellus 33:19-42.

within two to three days. Beyond three days, the curve flattens out and shows very little increase. If we define persistence as the lower limit of a useful forecast, then it can be seen that the low resolution (15R6) height forecasts have no skill beyond four days. The high-resolution height forecasts (30R12) are still useful at four days and probably retain some skill at six or seven days.

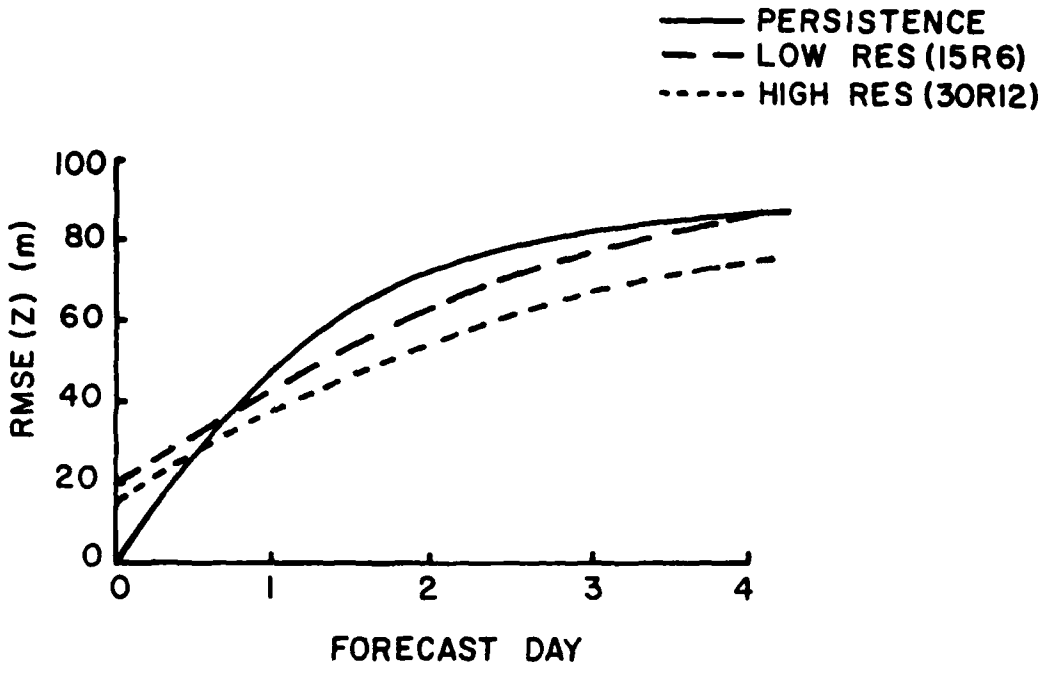

Figure 6. Growth Rate of the Average 1000-200 mb Height Errors for Six Forecasts (Three From January 1978 and Three From July 1978)

Figure 7 shows the error growth rate for the 850-mb relative humidity for the same six forecasts. In contrast to the other prognostic variables, relative humidity forecasts have no skill at all as measured by a comparison with persistence. Furthermore, very little difference exists between the errors of the low- and high-resolution forecasts. This indicates that, for reasons yet to be determined, there is a very strong tendency for the model-predicted humidity to quickly evolve to a certain preferred or "climatological" state that may differ substantially from the Hough-analyzed humidity. This characteristic seems to be common to

all global models.[7,8] The other interesting point to note in Figure 7 is the very small growth rate in persistence beyond day one. This lack of variation in the humidity analyses is probably due to the coarse resolution and poor quality of the Hough analysis scheme as applied to relative humidity.

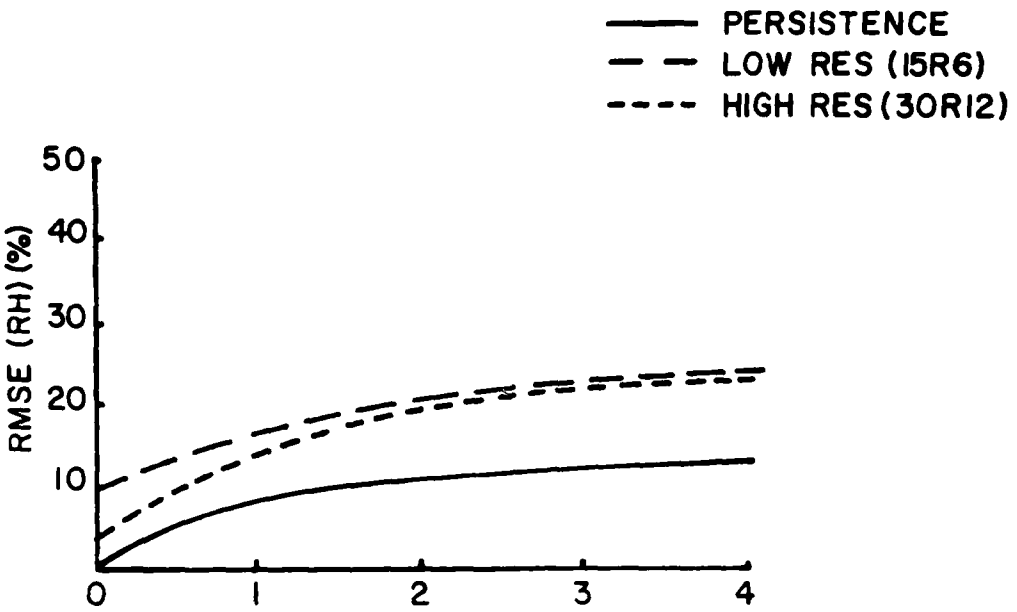

Figure 7. Growth Rate of the Average 850 mb Relative Humidity Errors for Six Forecasts (Three From January 1978 and Three From July 1978)

An example of the low- and high-resolution forecasts is shown in Figures 8, 9, 10, and 11. Each figure includes four northern hemisphere polar stereographic plots of height: (a), the verifying analysis, (b) the low resolution forecast (15R6), (c), the high resolution forecast (30R12), and (d) the difference between the high and low resolutions. The initial data consisted of the FGGE III-A analysis for 00Z 17 January 1978. Figures 8 and 9 show the 48-hour forecasts of the 1000 mb and 500 mb heights, respectively. At 48 hours, both resolutions can reasonably

---

7. Sirutis, J., Miyakoda, K., and Ploshay, J. (1980) Moisture distribution derived in mathematical models and four dimensional assimilation, in Atmospheric Water Vapor, Academic Press, New York, pp. 489-496.

8. Nieminen, R. (1983) Operational Verification of ECMWF Forecast Fields and Results for 1980-1981, ECMWF Technical Report No. 36.

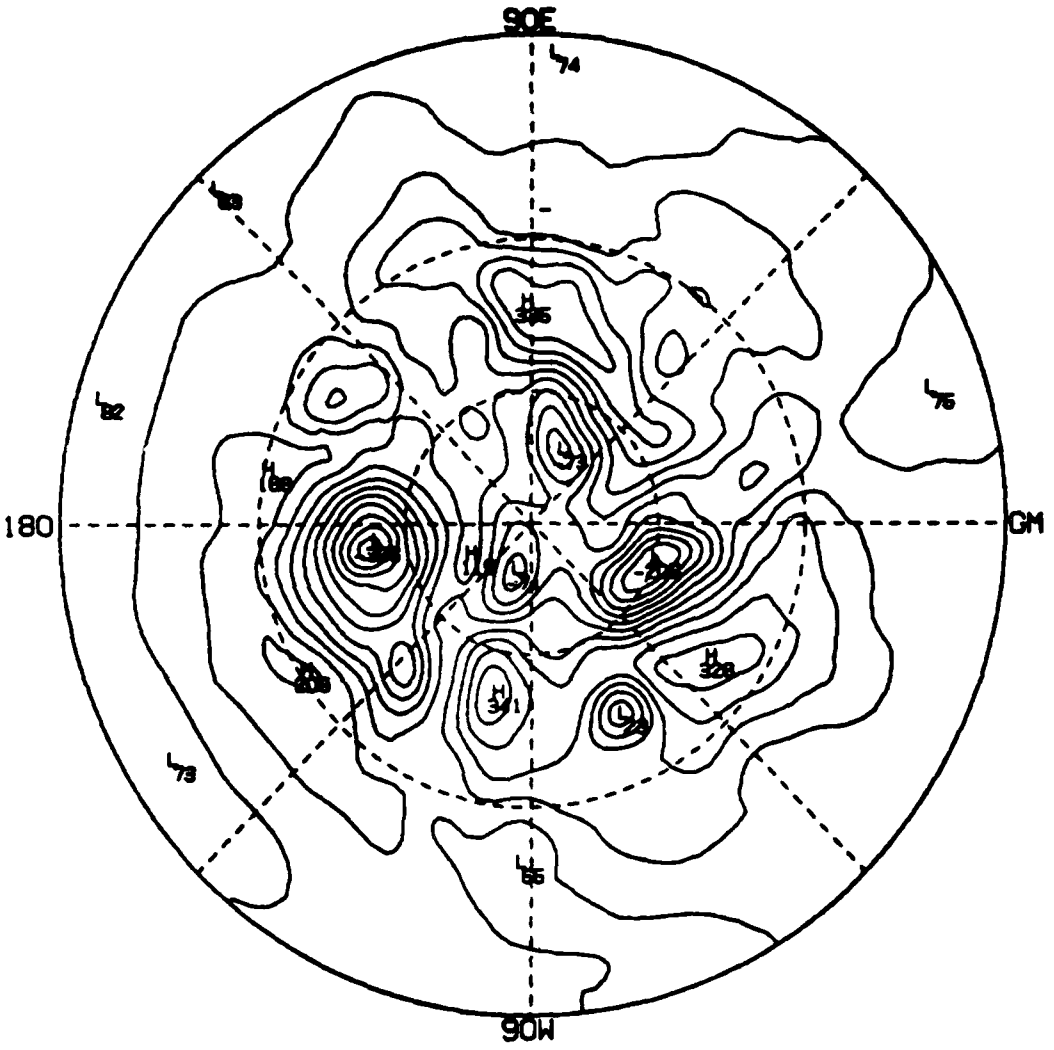

ANALYZED HEIGHT FIELD
1000 MB
00Z JAN 19, 1978

Figure 8a. 48-Hour Forecast of 1000 mb Heights Beginning From 00Z 17 January 1978: Verifying Analysis. Contour interval is 50 m

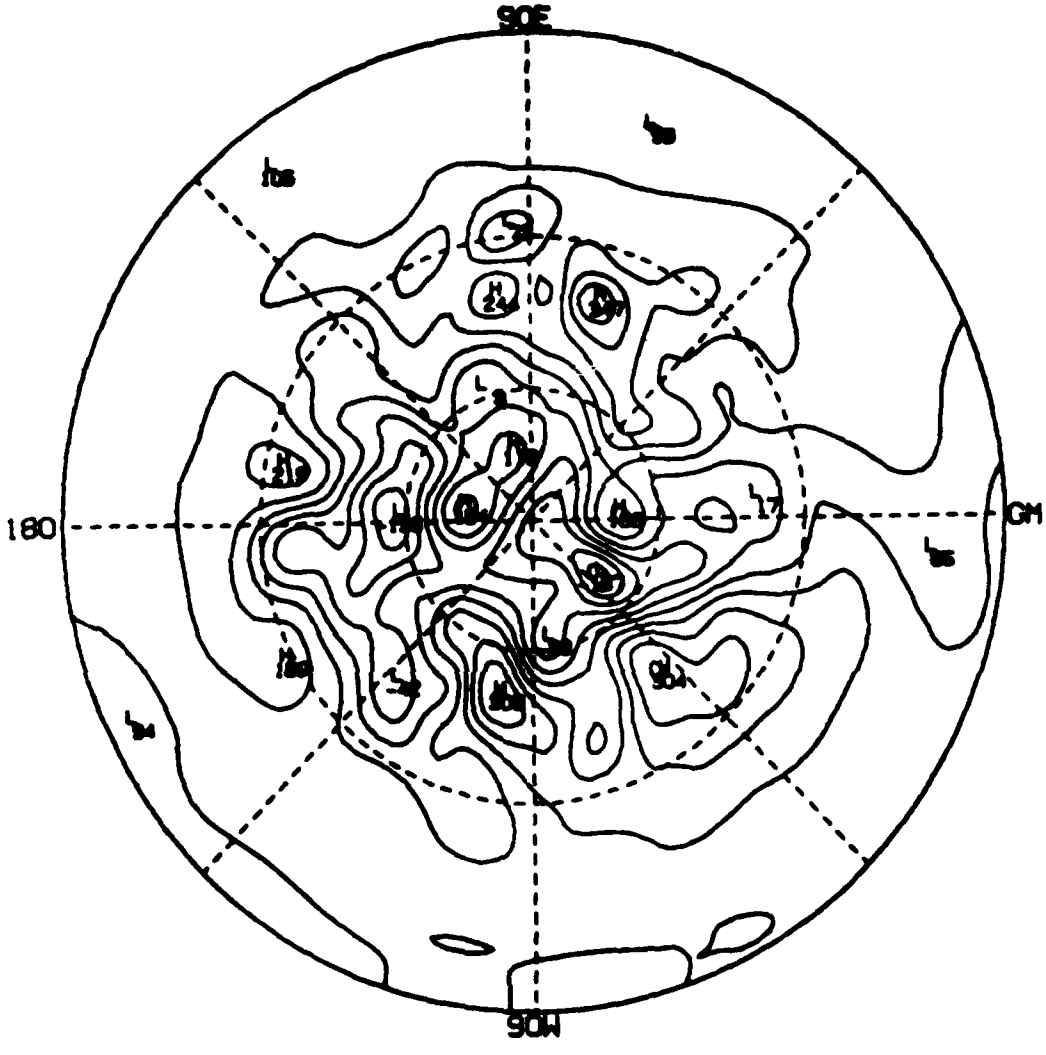

48 HR FORECAST HEIGHT FIELD LOW RESOLUTION
1000 MB
00Z JAN 19, 1978

Figure 8b. 48-Hour Forecast of 1000 mb Heights Beginning From 00Z 17 January 1978: Low Resolution (15R6). Contour interval is 50 m

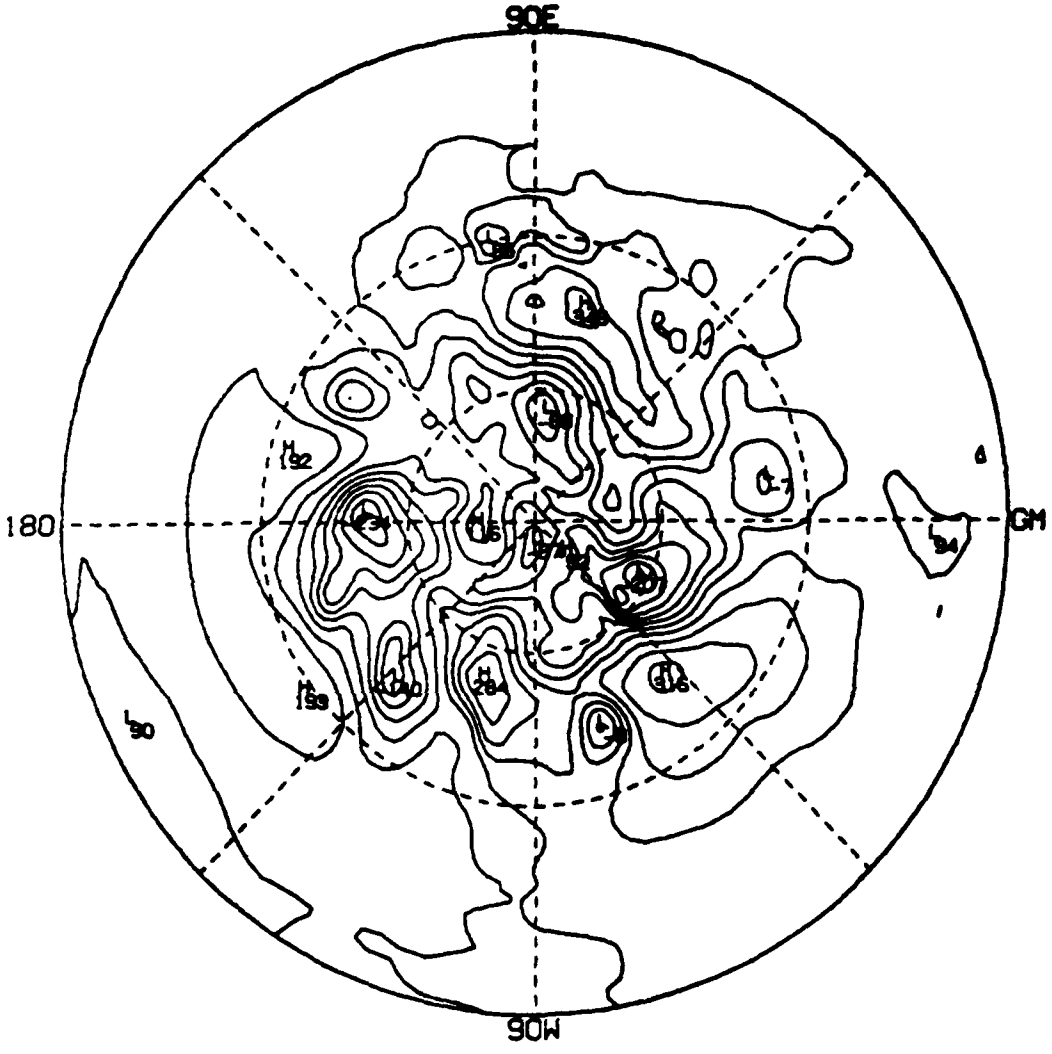

48 HR FORECAST HEIGHT FIELD HIGH RESOLUTION
1000 MB
00Z JAN 19, 1978

Figure 8c. 48-Hour Forecast of 1000 mb Heights Beginning From 00Z 17 January 1978: High Resolution (30R12). Contour interval is 50 m

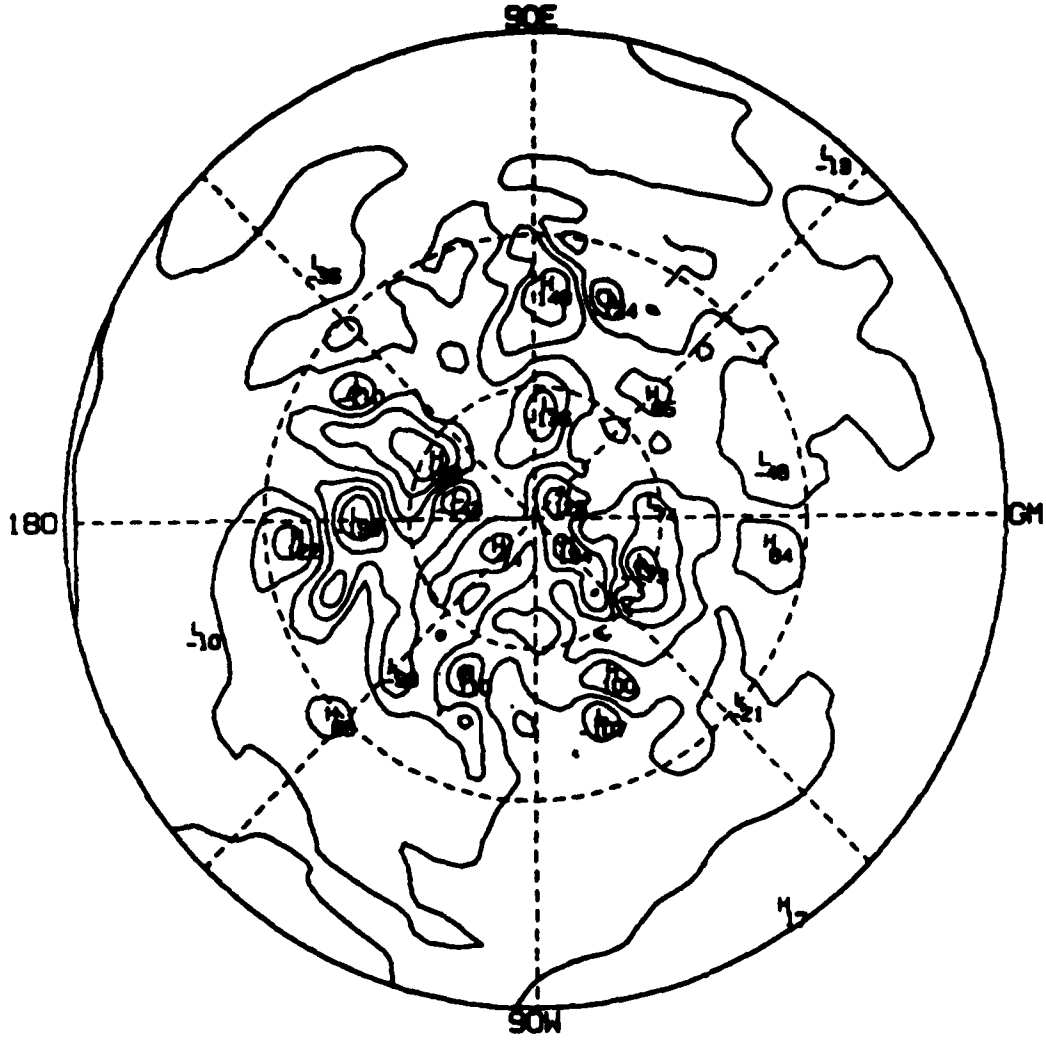

48 HR FORECAST HEIGHT DIFFERENCE BETWEEN HIGH
AND LOW RESOLUTIONS
1000 MB
00Z JAN 19, 1978

Figure 8d. 48-Hour Forecast of 1000 mb Heights Beginning From 00Z 17 January 1978: Difference Between High and Low Resolutions. Contour interval is 50 m

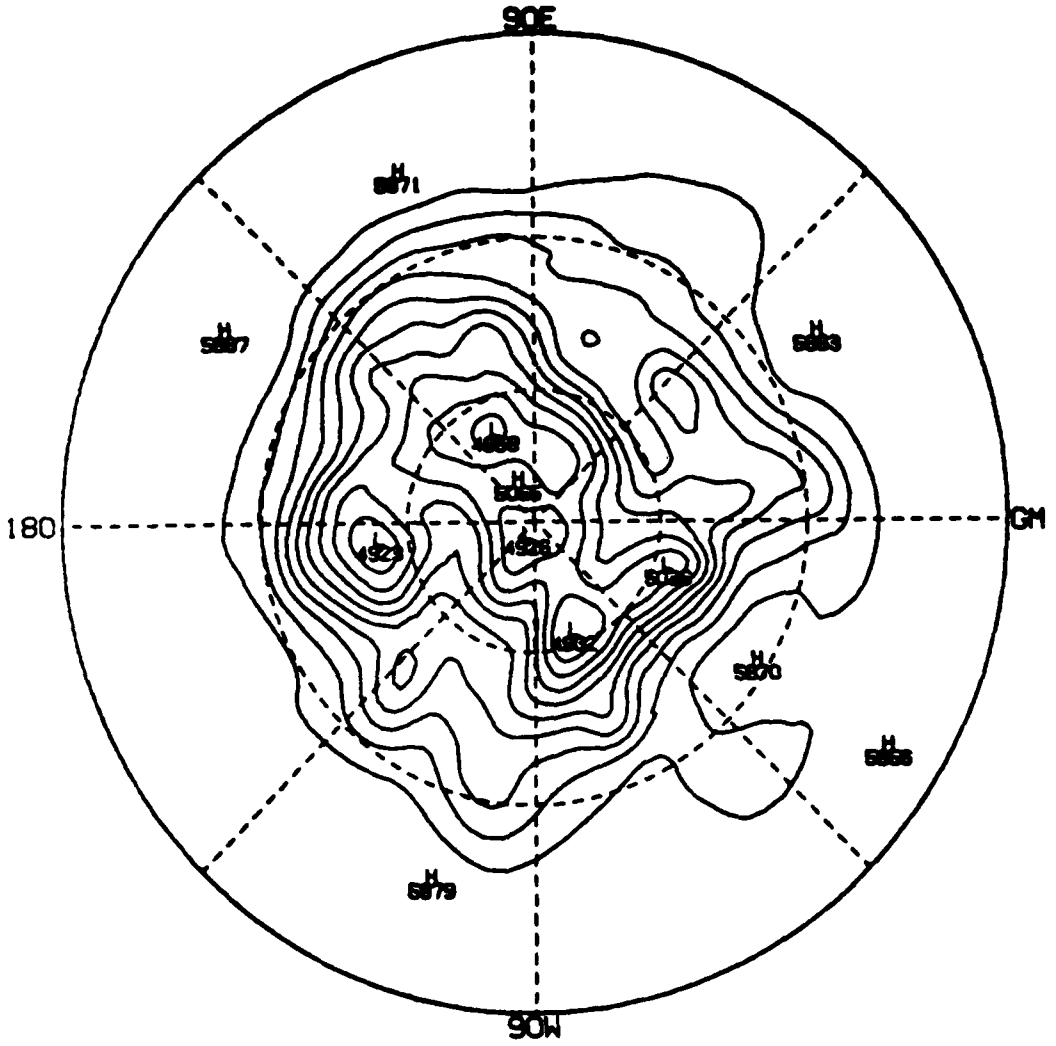

Figure 9a. 48-Hour Forecast of 500 mb Heights Beginning From 00Z 17 January 1978: Verifying Analysis. Contour interval is 50 m

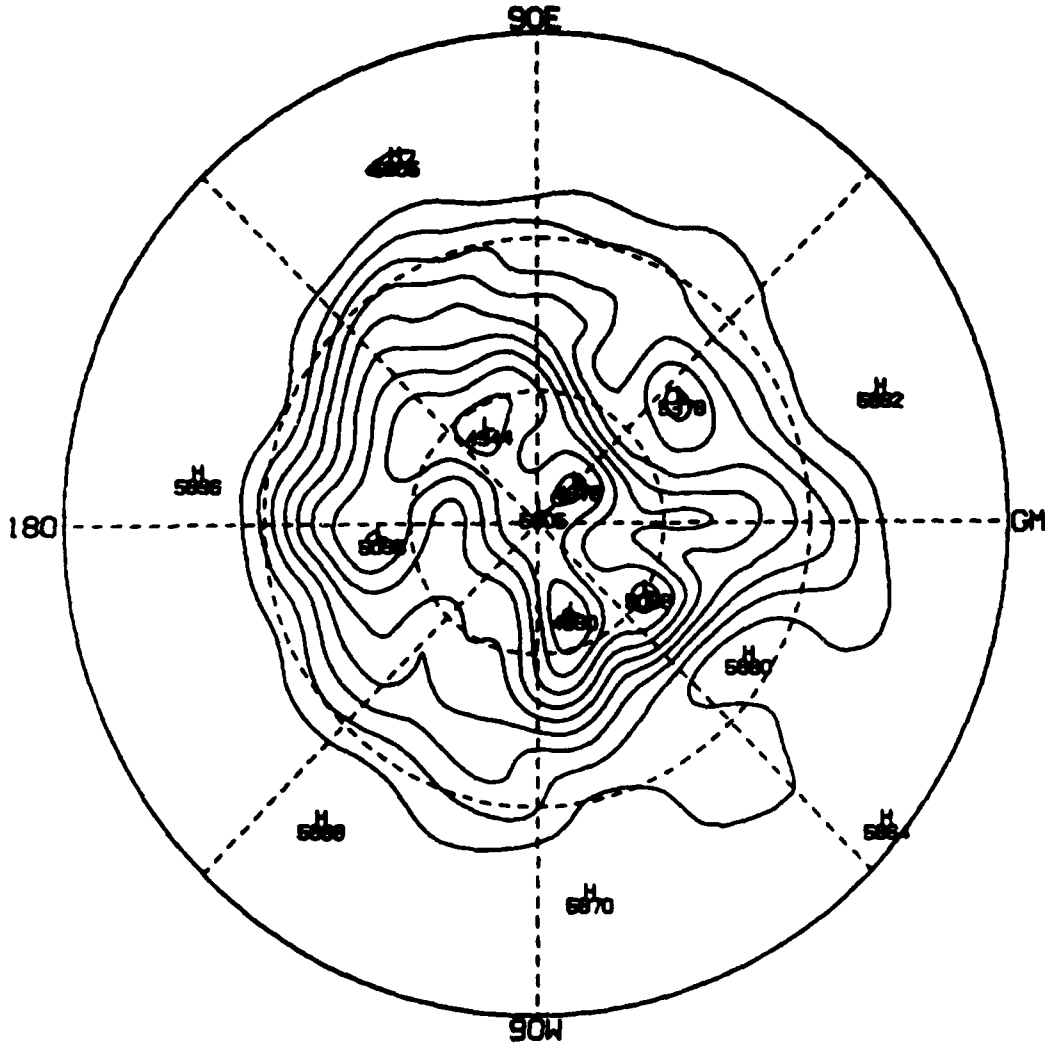

Figure 9b. 48-Hour Forecast of 500 mb Heights Beginning From 00Z 17 January 1978: Low Resolution (15R6). Contour interval is 50 m

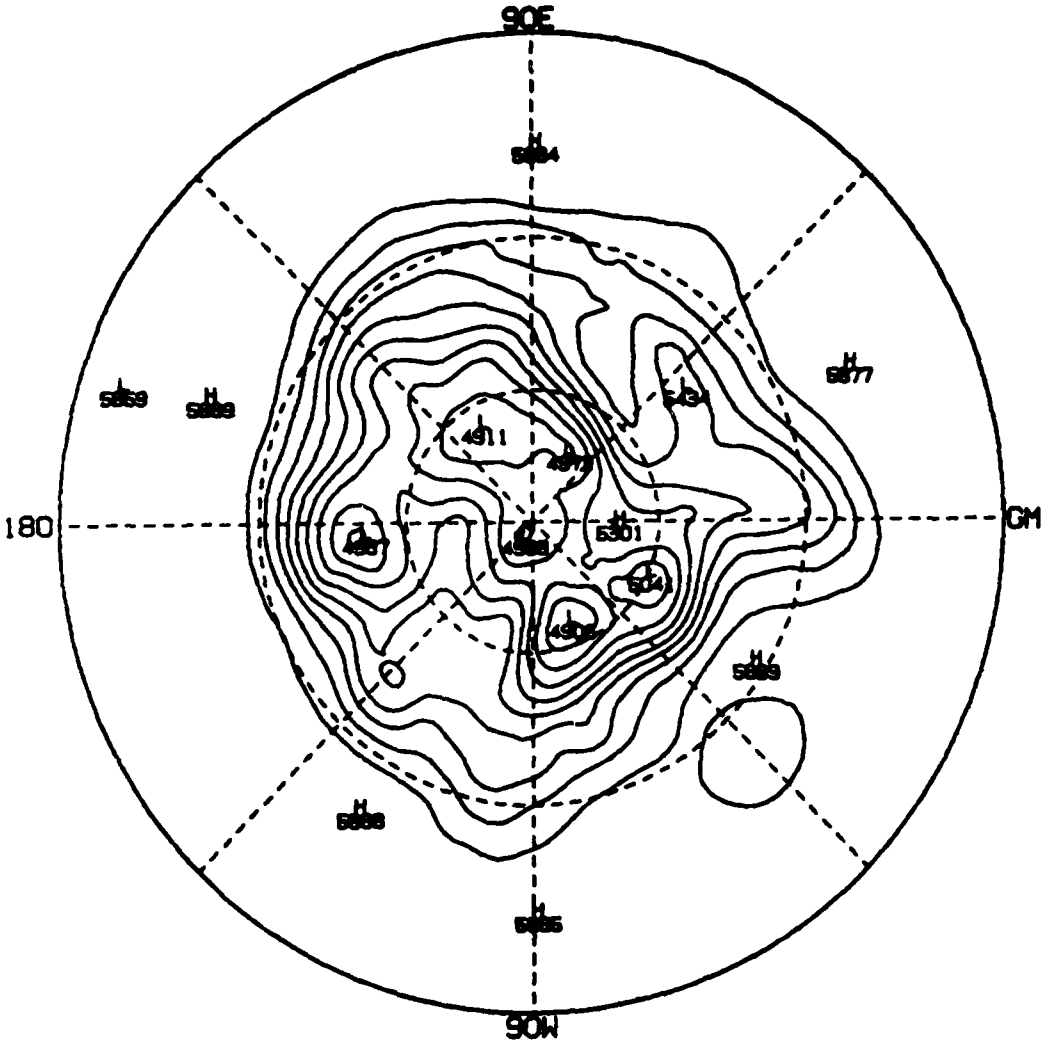

48 HR FORECAST HEIGHT FIELD HIGH RESOLUTION
500 MB
00Z JAN 19, 1978

Figure 9c. 48-Hour Forecast of 500 mb Heights Beginning From 00Z 17 January 1978: High Resolution (30R12). Contour interval is 50 m

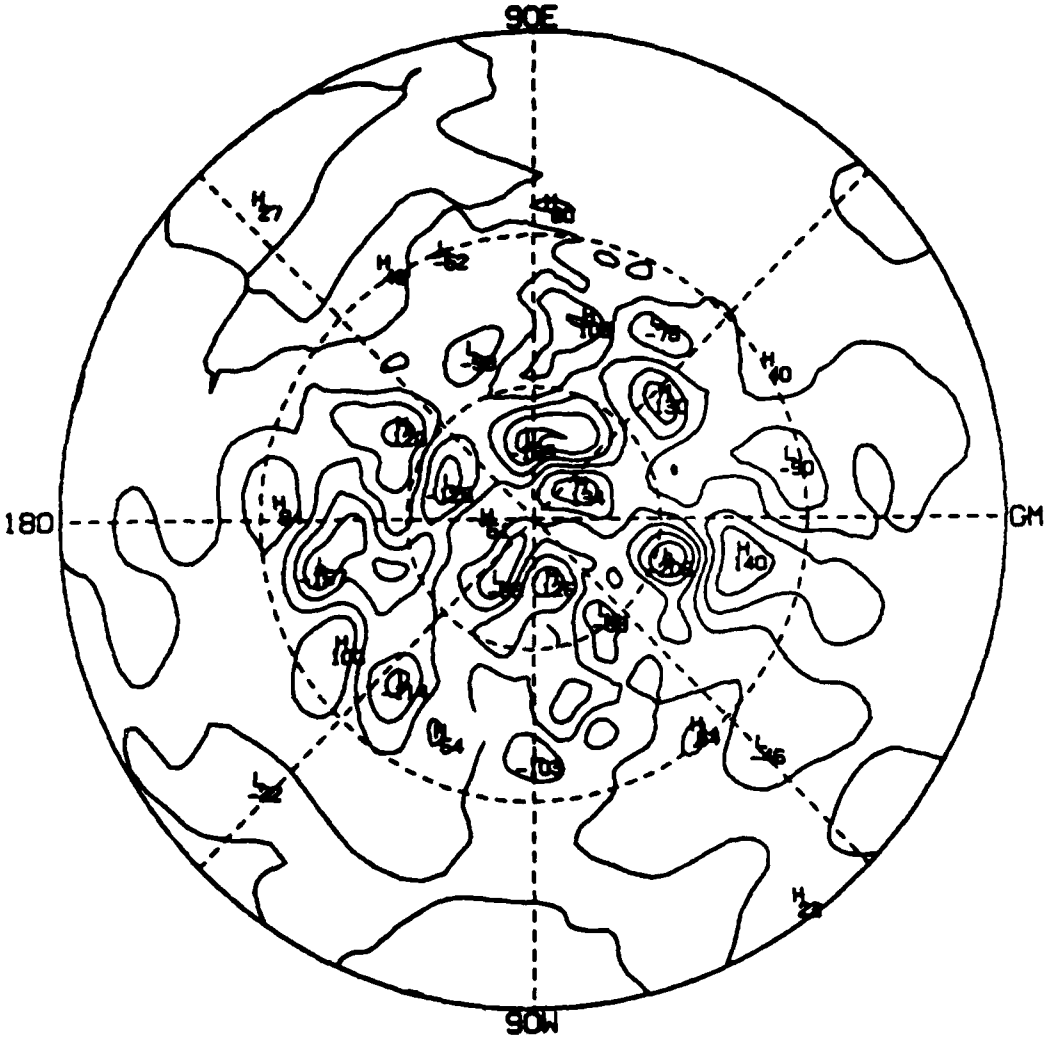

48 HR FORECAST HEIGHT DIFFERENCE BETWEEN HIGH AND LOW RESOLUTIONS
500 MB
00Z JAN 19, 1978

Figure 9d. 48-Hour Forecast of 500 mb Heights Beginning From 00Z 17 January 1978: Difference Between High and Low Resolutions. Contour interval is 50 m

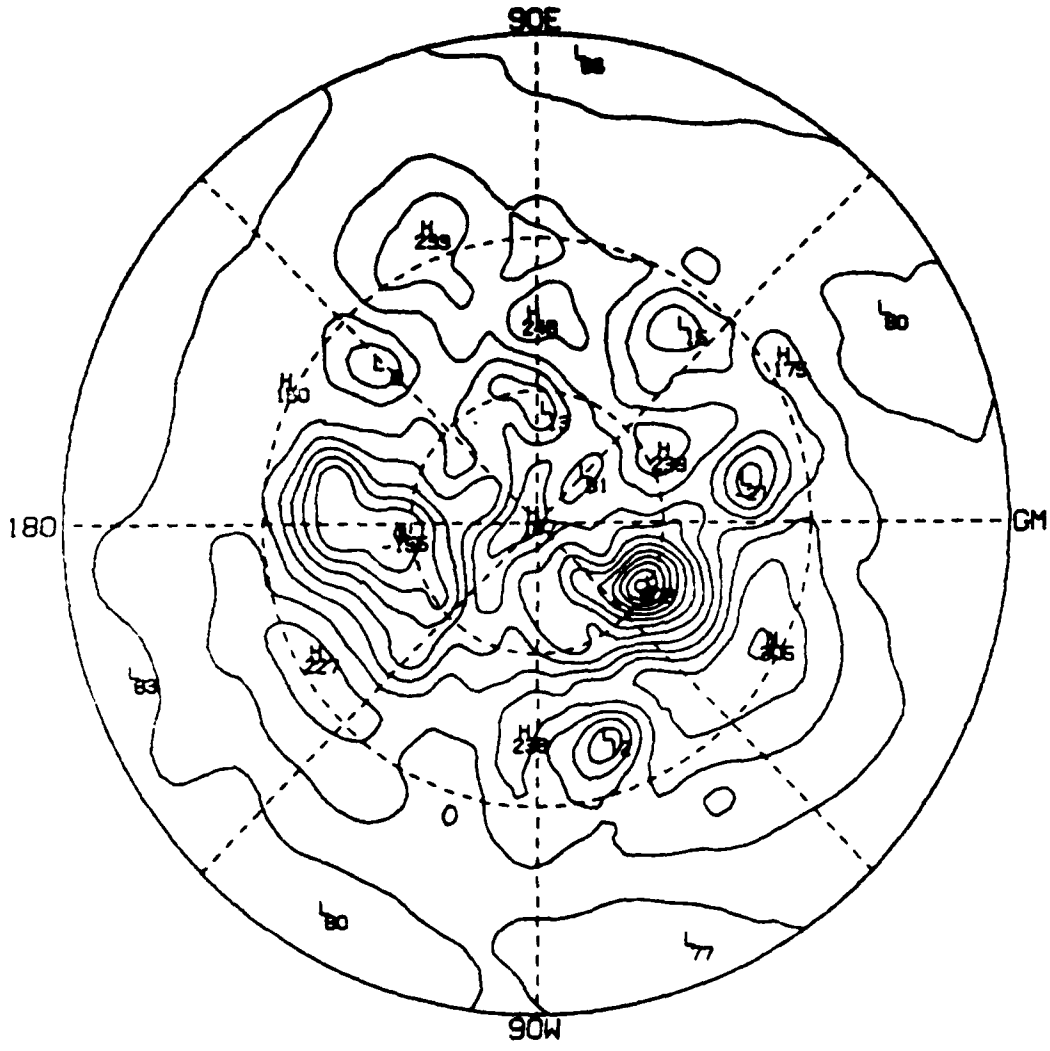

ANALYZED HEIGHT FIELD
1000 MB
00Z JAN 21, 1978

Figure 10a. 96-Hour Forecast of 1000 mb Heights Beginning From 00Z 17 January 1978: Verifying Analysis. Contour interval is 50 m

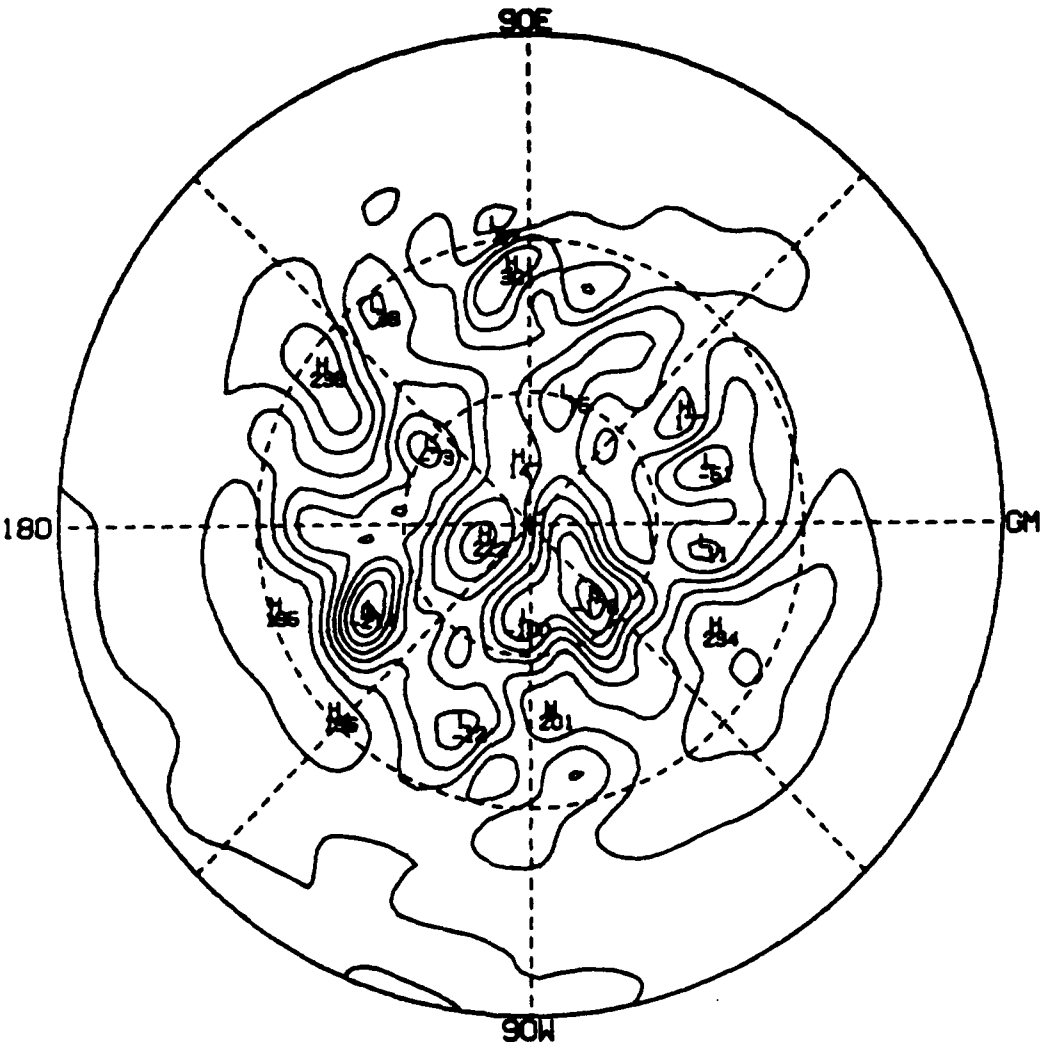

96 HR FORECAST HEIGHT FIELD LOW RESOLUTION
1000 MB
00Z JAN 21, 1978

Figure 10b. 96-Hour Forecast of 1000 mb Heights Beginning From 00Z 17 January 1978: Low Resolution (15R6). Contour interval is 50 m

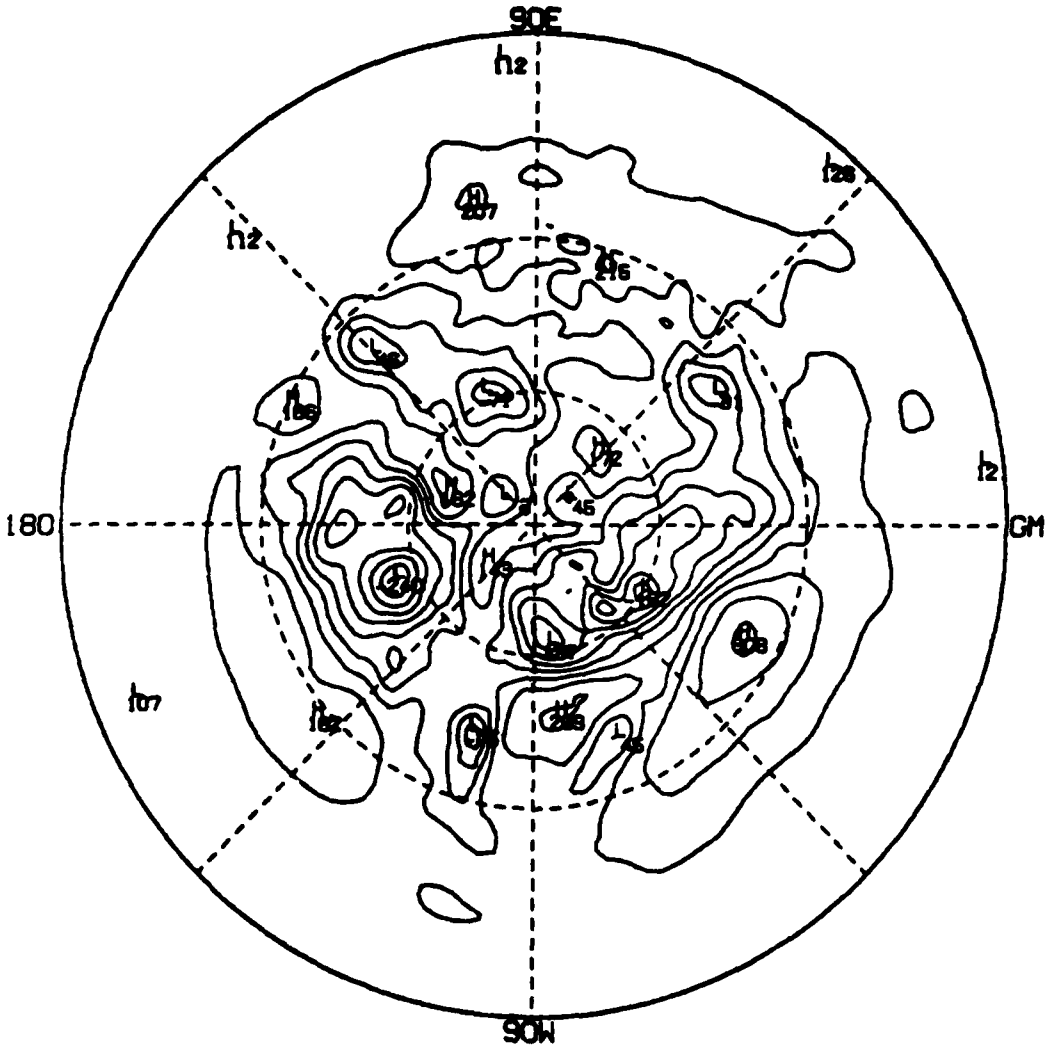

96 HR FORECAST HEIGHT FIELD HIGH RESOLUTION
1000 MB
00Z JAN 21, 1978

Figure 10c. 96-Hour Forecast of 1000 mb Heights Beginning From 00Z 17 January 1978: High Resolution (30R12). Contour interval is 50 m

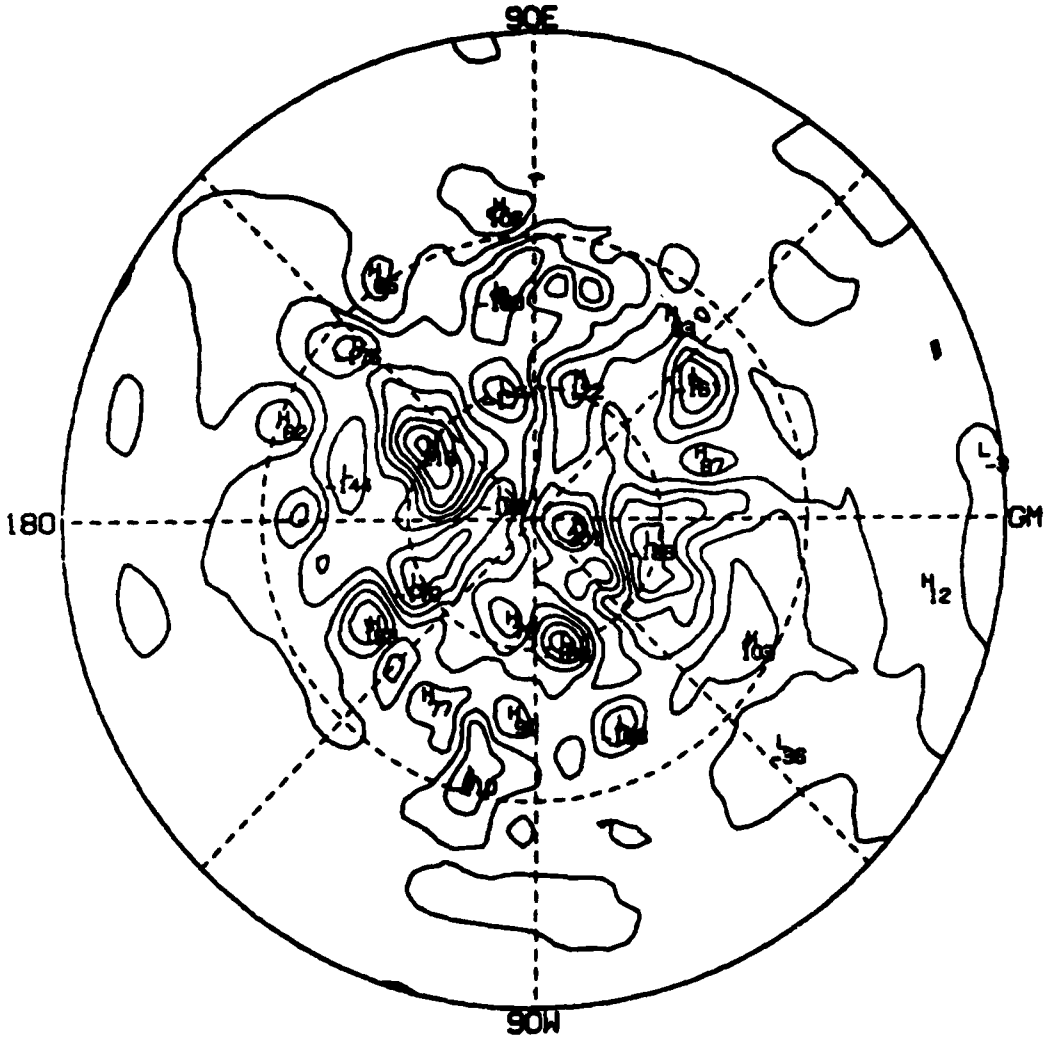

96 HR FORECAST HEIGHT DIFFERENCE BETWEEN HIGH
AND LOW RESOLUTIONS
1000 MB
00Z JAN 21, 1978

Figure 10d. 96-Hour Forecast of 1000 mb Heights Beginning From 00Z 17 January 1978: Difference Between High and Low Resolutions. Contour interval is 50 m

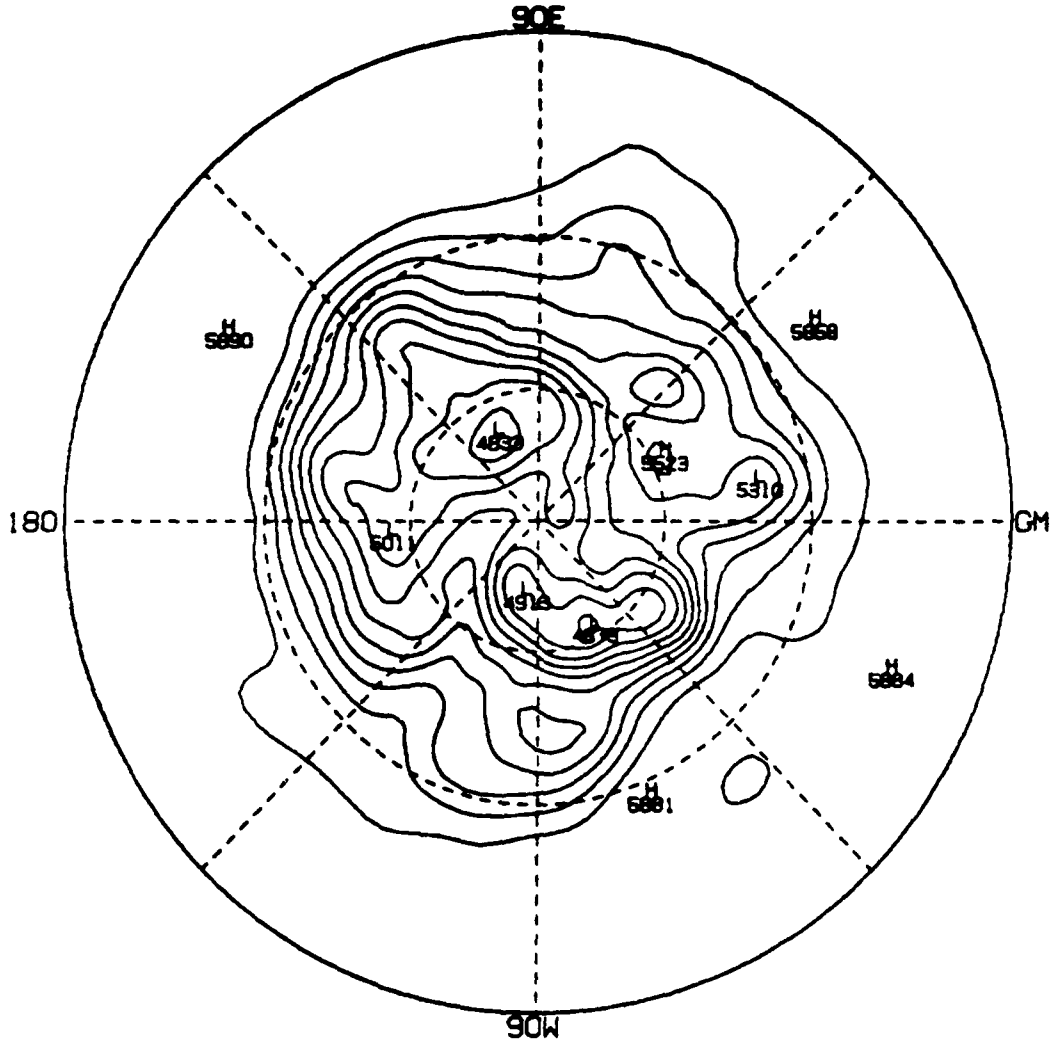

ANALYZED HEIGHT FIELD
500 MB
00Z JAN 21, 1978

Figure 11a. 96-Hour Forecast of 500 mb Heights beginning From 00Z 17 January 1978: Verifying Analysis. Contour interval is 50 m

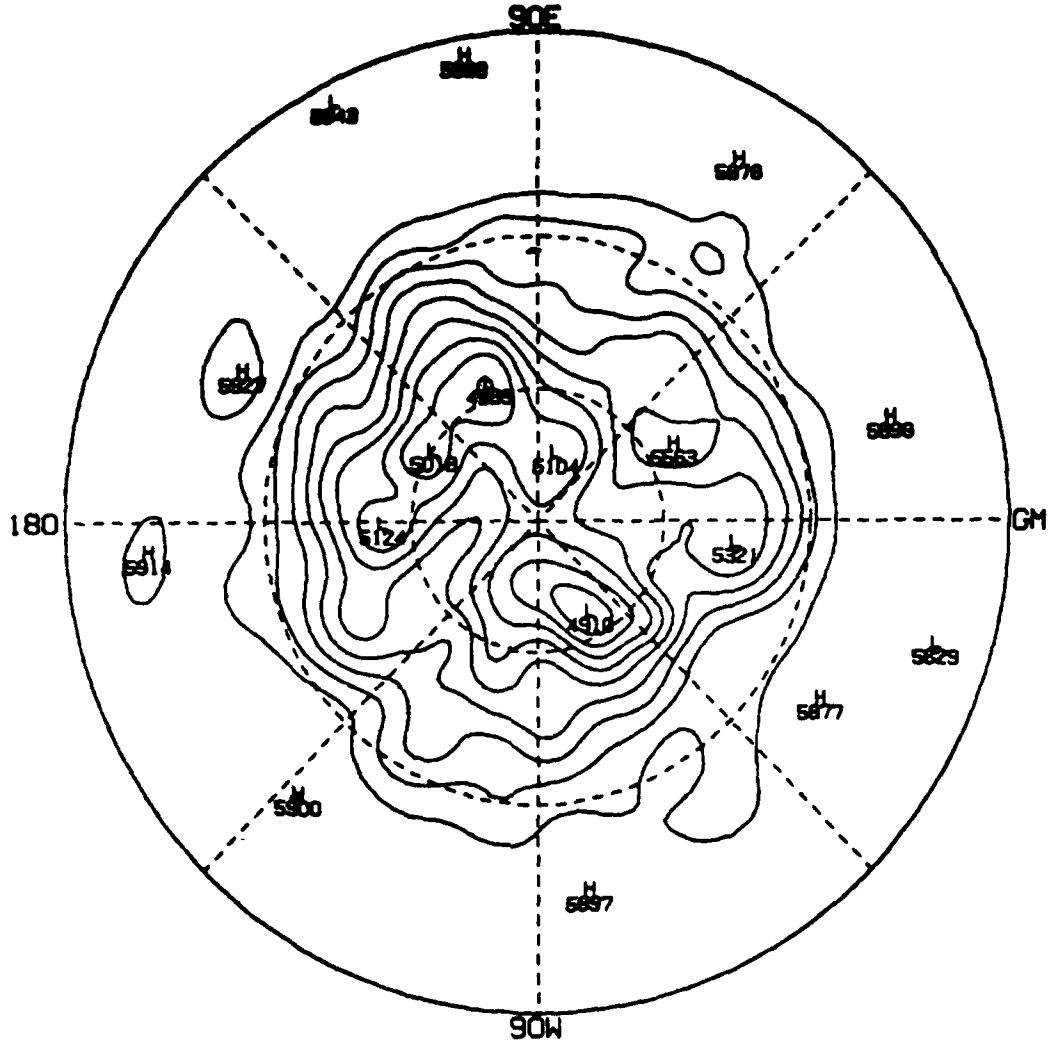

Figure 11b. 96-Hour Forecast of 500 mb Heights Beginning From 00Z 17 January 1978: Low Resolution (15R6). Contour interval is 50 m

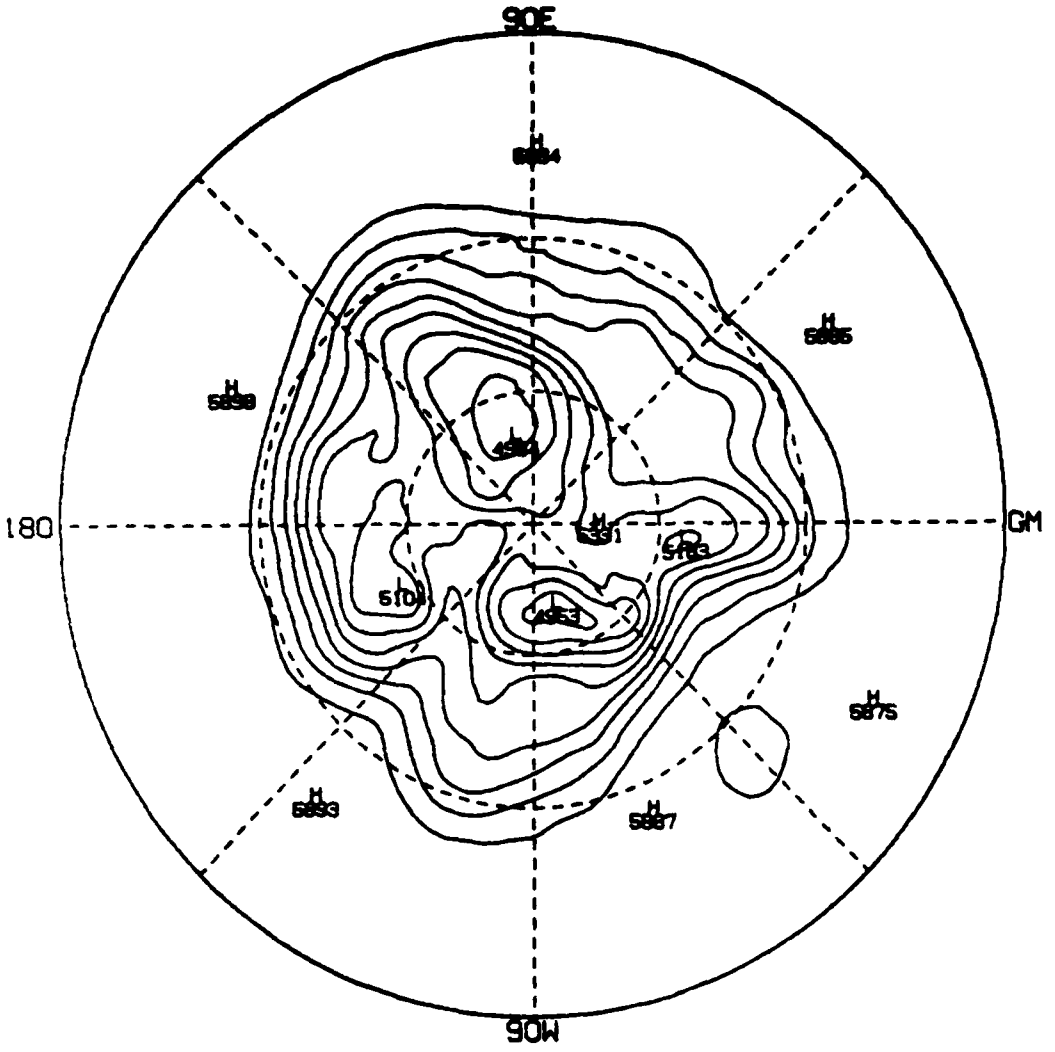

96 HR FORECAST HEIGHT FIELD HIGH RESOLUTION
500 MB
00Z JAN 21, 1978

Figure 11c. 96-Hour Forecast of 500 mb Heights Beginning From 00Z 17 January 1978: High Resolution (30R12). Contour interval is 50 m

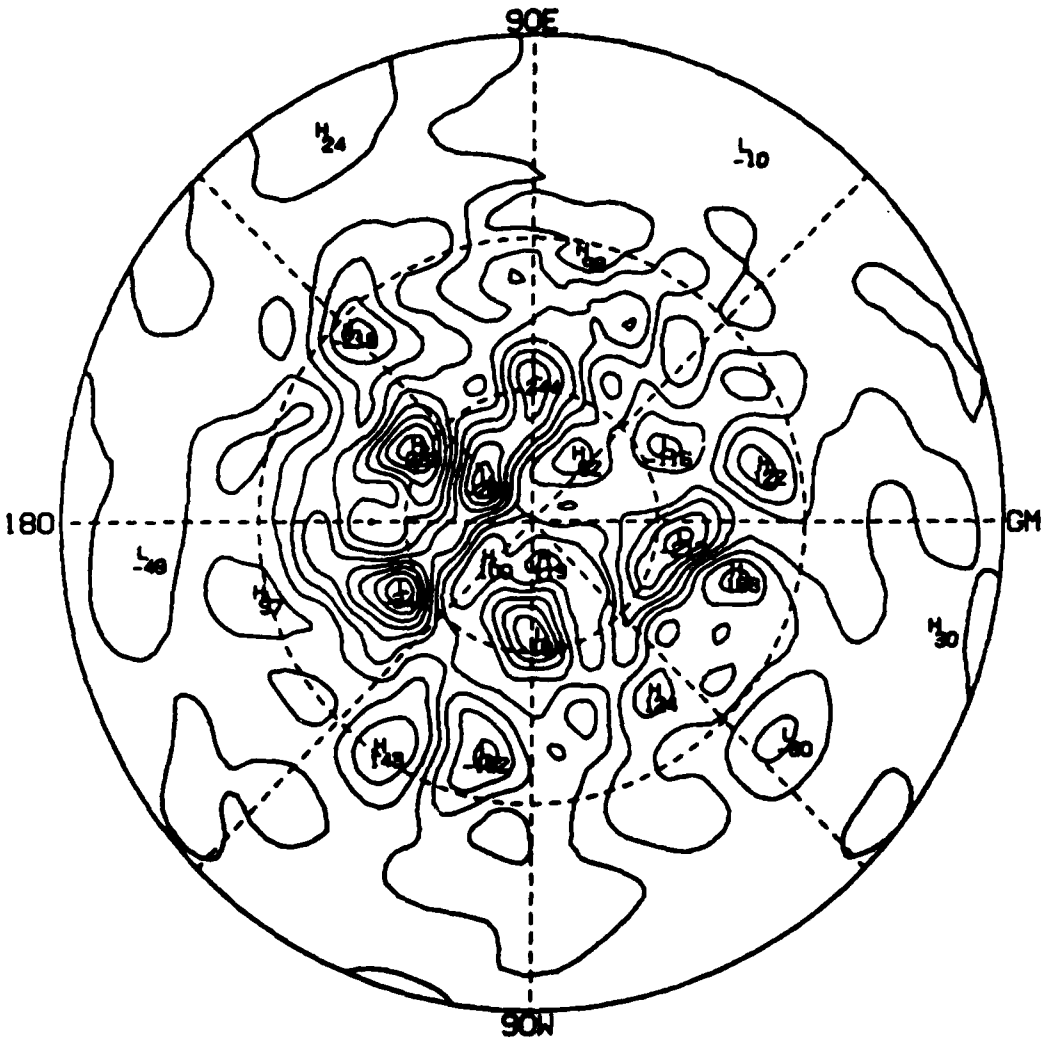

96 HR FORECAST HEIGHT DIFFERENCE BETWEEN HIGH
AND LOW RESOLUTIONS
500 MB
00Z JAN 21, 1978

Figure 11d. 96-Hour Forecast of 500 mb Heights Beginning From 00Z 17 January 1978: Difference Between High and Low Resolutions. Contour interval is 50 m

forecast the locations of the major pressure systems. In general, however, the amplitudes in the low-resolution forecast tend to be too small. This is most noticeable in the strong cyclone that has developed over the mid-Pacific (at both 1000 and 500 mb). Also, the low-resolution forecast cannot adequately capture smaller scale features such as fronts.

Figures 10 and 11 show the 96-hour forecasts of the 1000 mb and 500 mb heights, respectively. Here, the differences in resolution become much more apparent. The low-resolution forecast has lost most of its predictive skill (also see Figure 12) and begins to suffer from both amplitude and phase errors. This is especially noticeable in the 500 mb forecast and in the differences between the high and low resolution forecasts (Figure 11d).

Finally, in Figure 12, we show the growth rates of the height errors at (a) 1000 mb, (b) 500 mb, (c) 250 mb, and (d) average 1000-200 mb. In general, the difference in skill between the low- and high-resolution forecasts increases with time and altitude. The extremely poor performance of the low-resolution forecast at 250 mb is caused primarily by the lack of adequate vertical resolution in the upper troposphere and lower stratosphere.

7. REPRESENTATION OF TOPOGRAPHY

The basic source of information on the surface topography is a set of height values on the 2.5° -interval latitude-longitude coordinates furnished by NMC as a part of the fixed field data in the FGGE III-A data set. It is assumed that the value at each grid point has been obtained through an averaging process and represents the mean terrain height of the area over which the average has been defined. The network of grid points on which various calculations are performed in a spectral model is generally different, from the network of grid points in the basic data set. Consequently, a question arises about how the representation of the surface topography in a spectral model of specified resolution should be generated from the basic data.

The theory of linear transformations shows that any set of real-valued data $(X(\lambda_j, \theta_\ell), j = 1, \ldots, J; \ell = 1, \ldots L)$ such as topography may be represented through the Fourier transform by an analytic function

$$\tilde{X}(\lambda, \phi) = \sum_{m=-M}^{M} Q_m (\sin\phi)\ e^{im\lambda} \tag{29}$$

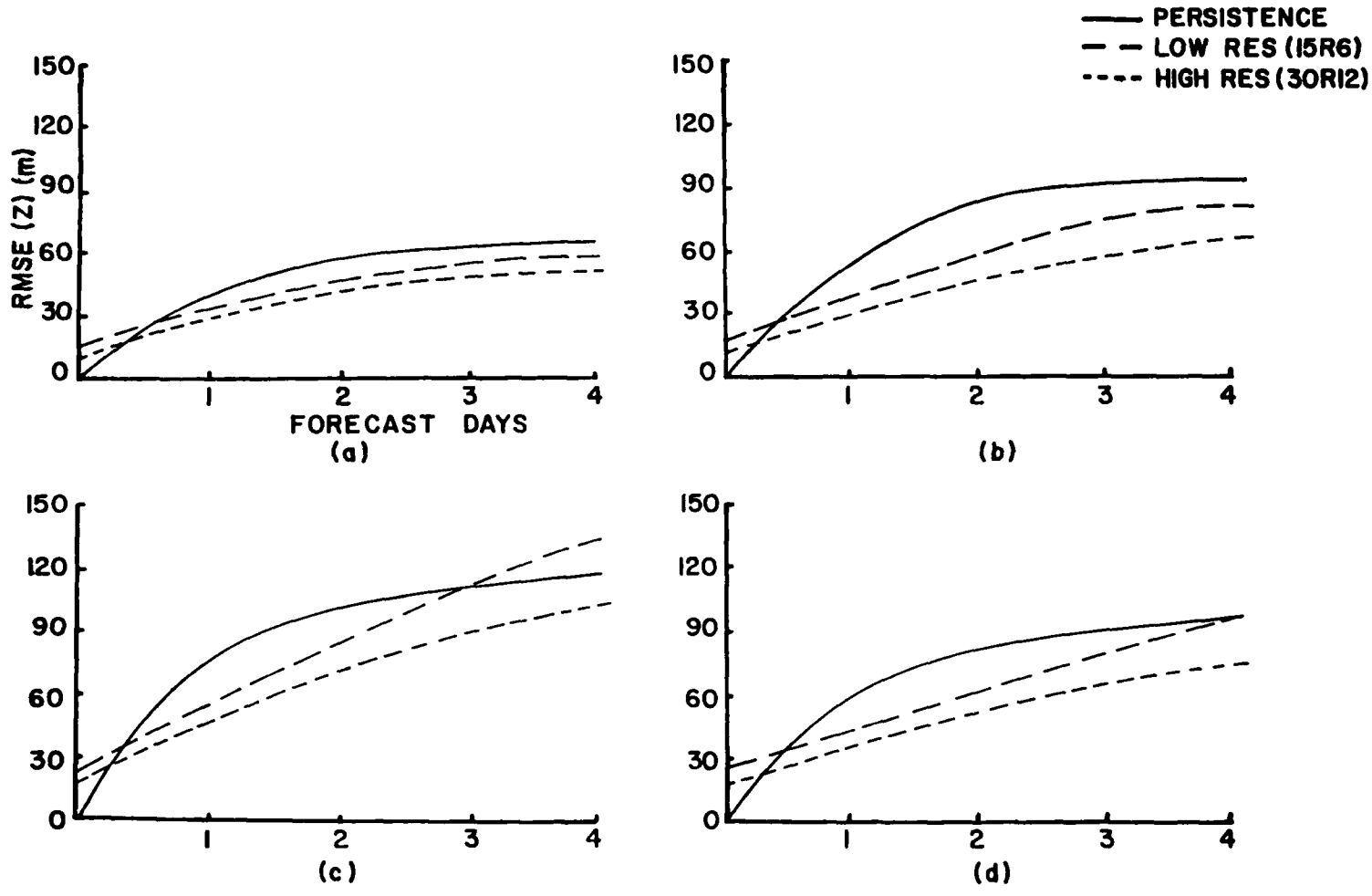

Figure 12. Growth Rate of Height Errors for Forecasts From 00Z 17 January 1978: (a) 1000 mb, (b) 500 mb, (c) 250 mb, and (d) Average 1000-200 mb

such that $X(\lambda_j, \phi_\ell) = \tilde{X}(\lambda_j, \phi_\ell)$ at all j and ℓ. Here, M = J/2 (when J is even) or (J-1)/2 (when J is odd), and $Q_m(\sin\phi)$ is a polynomial of degree (L-1) in $\sin\phi$ for each m such that Q_{-m} and Q_m form a complex conjugate pair.

The analytic function $\tilde{X}(\lambda, \phi)$, on the other hand, may be represented in terms of spherical harmonics,

$$\tilde{X}(\lambda, \phi) = \sum_{m=-M}^{M} \sum_{n=|m|}^{\infty} X_n^m \; P_n^m(\sin\phi) \; e^{im\lambda} \tag{30}$$

in which

$$X_n^m = \int_{-1}^{1} Q_m(y) \; P_n^m(y) \; dy$$

where

$$\int_{-1}^{1} P_n^m(y) \; P_{n'}^m(y) \, dy = \delta_{nn'} \tag{31}$$

for all m, $y = \sin\phi$, and $\delta_{nn'}$ is the Kronecker delta. The integral in Eq. (31) will be referred to as "the Legendre transform." The integrand in Eq. (31) is seen to be

$$Q_m(y) P_n^m(y) = \begin{cases} \text{a polynomial in y of degree } (L+n-1) \\ \text{when m is even;} \\ (1-y^2)^{1/2} \text{ times a polynomial in y of} \\ \text{degree } (L+n-2) \text{ when m is odd.} \end{cases}$$

In practice, the wave amplitudes at a given latitude ϕ_ℓ are first obtained from $(X(\lambda_j, \phi_\ell), j = 1, \ldots, J)$ using the Fourier transform

$$Q_m(\phi_\ell) = \sum_{j=1}^{J} X(\lambda_j, \phi_\ell) \; e^{-im\lambda_j} \tag{32}$$

and then the integral in Eq. (31) is replaced by a quadrature which may be written as

$$\hat{X}_n^m = \sum_{\ell=1}^{L} Q_m(y_\ell) \; P_n^m(y_\ell) \; w_\ell \tag{33}$$

where $y_\ell = \sin\phi_\ell$ and w_ℓ is the weight associated with y_ℓ. The reconstructed topography becomes

$$\hat{X}(\lambda, \phi) = \sum_{m=-M_o}^{M_o} \sum_{n=|m|}^{N_o} \hat{X}_n^m \, P_n^m(y) \, e^{im\lambda} \tag{34}$$

in which M_o and N_o define the range of truncation. The error of spectral synthesis, $X(\lambda_j, \phi_\ell) - \hat{X}(\lambda_j, \phi_\ell)$, is seen to arise from two possible sources, one in the quadrature [Eq. (33)] and the other in the truncation [Eq. (34)].

The impacts of quadrature and truncation on the representation of topography were examined by comparing various truncations in Eq. (34) and by using the trapezoidal and Gauss-Legendre (G-L) quadratures in Eq. (33). The trapezoidal quadrature assumes that the variation of the integrand between any two consecutive data points is linear, while the G-L quadrature with N Gaussian coordinates evaluates the integral accurate to the polynomial of degree 2N - 1. The former adapts itself to given data distributions, while the latter requires data on specific coordinates dictated by the degree of accuracy. The impact was measured by the global rms error, E, defined by

$$E = \left[\frac{\sum_\ell \sum_j \left\{ \hat{X}(\lambda_j, \phi_\ell) - X(\lambda_j, \phi_\ell) \right\}^2 w_j}{\sum_\ell \sum_j w_{j\ell}} \right]^{1/2} \tag{35}$$

where $w_{j\ell} = w_\ell$ in view of the fact that grid points are uniformly spaced around a latitude circle. When using the G-L quadrature, if the original terrain data are not on Gaussian latitudes, it is necessary to estimate the values of terrain height on the Guassian latitude at the corresponding longitudes. This was done by a linear interpolation in $\sin\phi$ using the two consecutive data latitudes that surround the Gaussian latitude of concern. The procedures encountered and quantities defined in a full cycle of transformation are illustrated and designated in Figures 13a, 13b, and 13c.

In view of the limited invertibility of the numerical quadratures for the Legendre transform, three measures of differences were used to characterize various aspects of the impacts of quadrature and truncation on the process of transformation. E_1 is the conventional error of synthesis and measures the combined impact of quadrature and truncation. E_2, on the other hand, measures the error incurred in completing a full circle of the transformation at a fixed truncation and represents the error entirely due to quadrature. Both E_1 and E_2 are

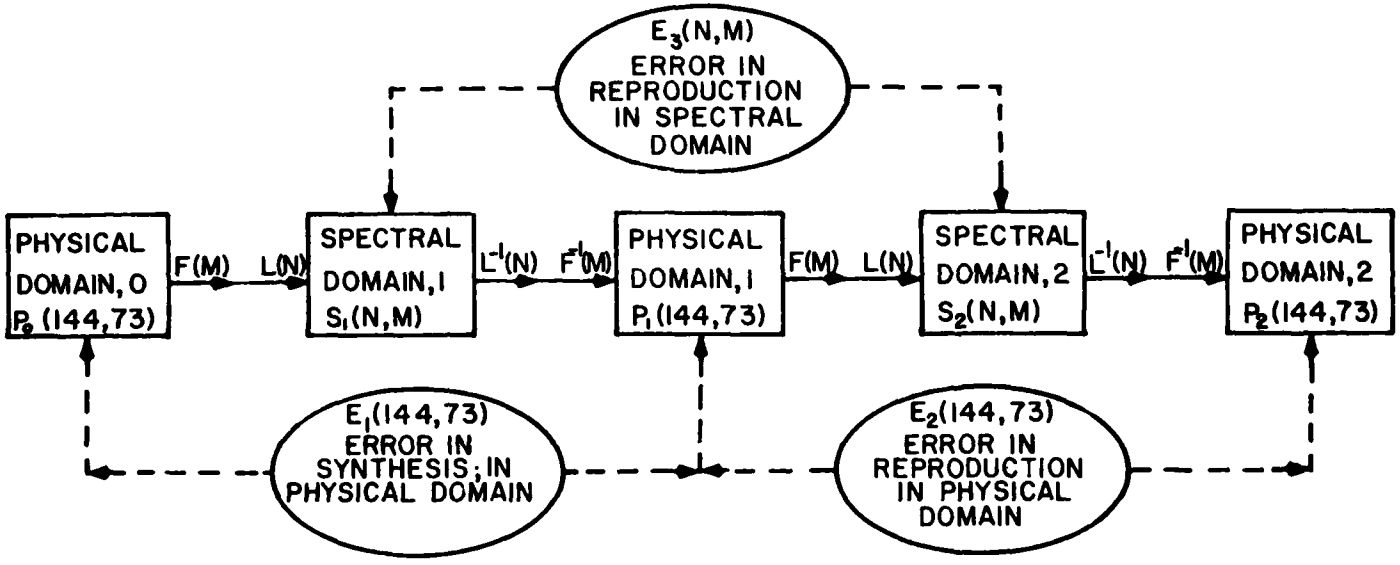

Figure 13a. Definitions of Quantities, Processes, and Errors in Representation of Topography Using Trapezoidal Quadrature

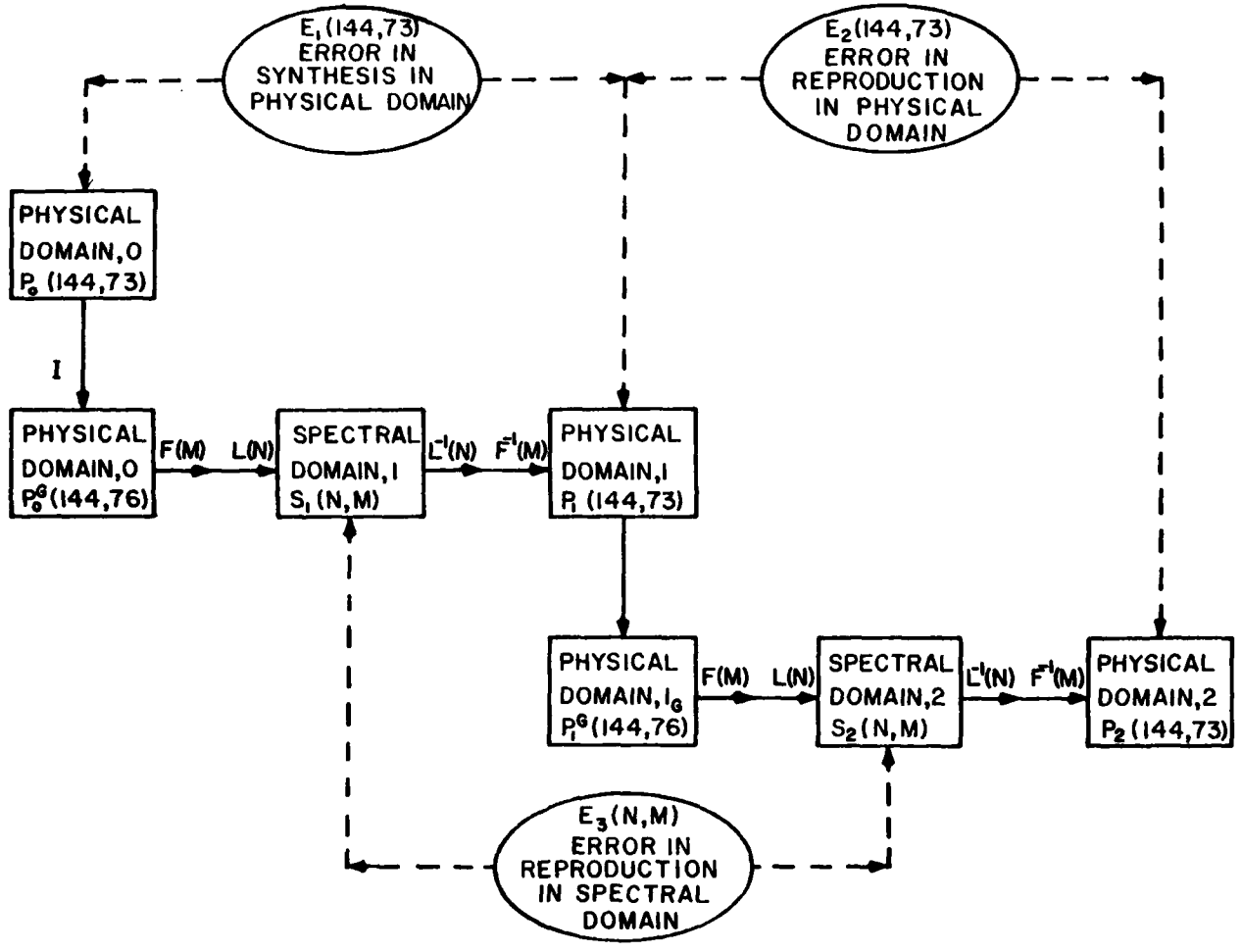

Figure 13b. Definitions of Quantities, Processes, and Errors in Representation of Topography Using Gaussian Quadrature, Data on Equally Spaced Latitudes

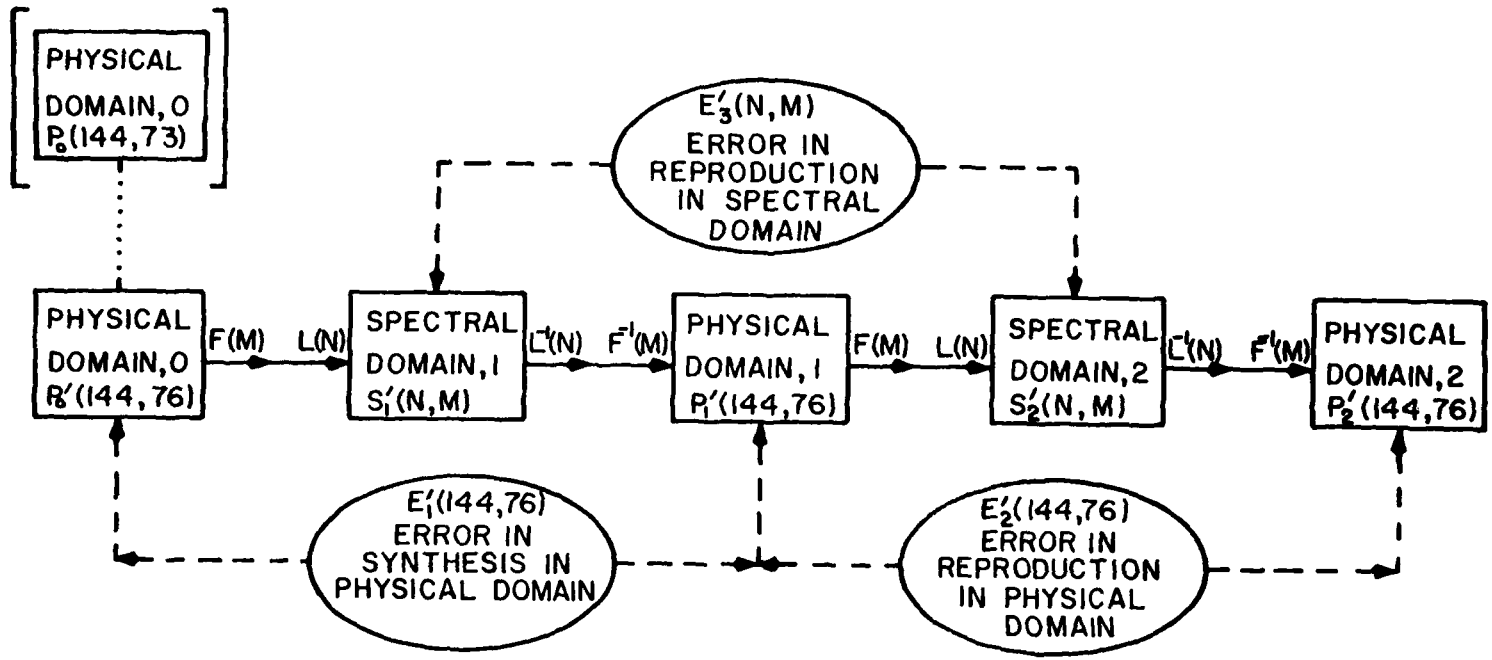

Figure 13c. Definitions of Quantities, Processes, and Errors in Representation of Topography Using Gaussian Quadrature, Data on Gaussian Latitudes

defined in the physical domain. The third measure, E_3, is an equivalent of E_2 in the spectral domain and will be identical in the total magnitude with E_2 when the spectral transform is exactly invertible. The composition of E_3 reveals the spectral distribution of the error of transformation due to quadrature. Additionally, in order to separate the effect of the required interpolation from the original data to the Gaussian latitudes from the effect of the G-L quadrature, similar measures of differences are defined with reference to the estimates on the Gaussian latitudes and are denoted by primes (Figure 13c).

These processes of transformation were applied to two fields of topography. The so-called unsmoothed terrain is the one given in the FCGE III-A data set. The so-called smoothed terrain has been obtained by subjecting the unsmoothed terrain to a nine-point smoother twice. The smoother is a product of two three-point smoothers, one along the zonal direction and the other in the meridonial direction. It may be represented by a linear operator W: $X = W\{\tilde{X}_{j,\ell}\}$ defined by $W(i, k: j, \ell) = w(i:j)\ w(k:\ell)$
where

$$w(i:j) = \begin{cases} 1/2 \text{ if } i = j \\ 1/4 \text{ if } i = j \pm 1 \\ 0 \text{ otherwise} \end{cases}$$

and similarly for $w(k:\ell)$.
Such a smoother has a progressively strong damping effect toward short waves and completely eliminates the two-grid interval wave. This is clearly evident in Table 7 which presents the amounts of variance contributed by various spectral ranges in both the unsmoothed and smoothed terrains. These spectra were obtained using the G-L quadrature. The meridional profiles of three parameters of these terrain fields are shown in Figures 14a and 14b. Here, DM, represented

Table 7. Amounts of Variance in Various Spectral Ranges in the Unsmoothed and Smoothed Terrains (Units of m^2)

Spectral Range	16 ≤ M < 24	25 ≤ M < 30	31 ≤ M < 40	41 ≤ M < 50	51 ≤ M < 60	61 ≤ M < 70
unsmoothed terrain	27955	9507	8379	5422	3384	3270
smoothed terrain	206	1632	562	195	93	51

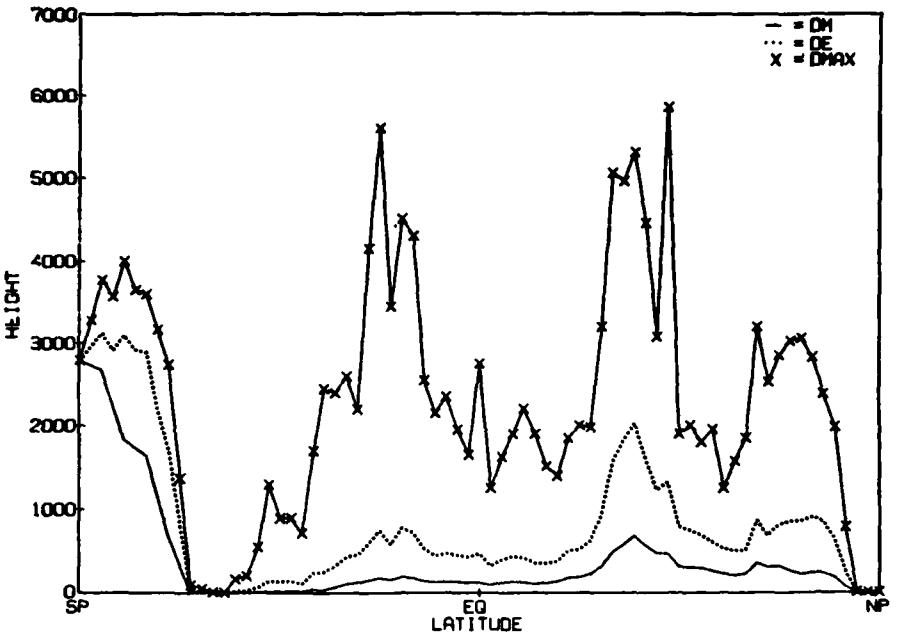

Figure 14a. Meridional Profiles of Terrain Parameters: DM-Zonal Mean, DE-Zonal Mean Plus Standard Deviation, DMAX-Maximum Value for Unsmoothed Terrain

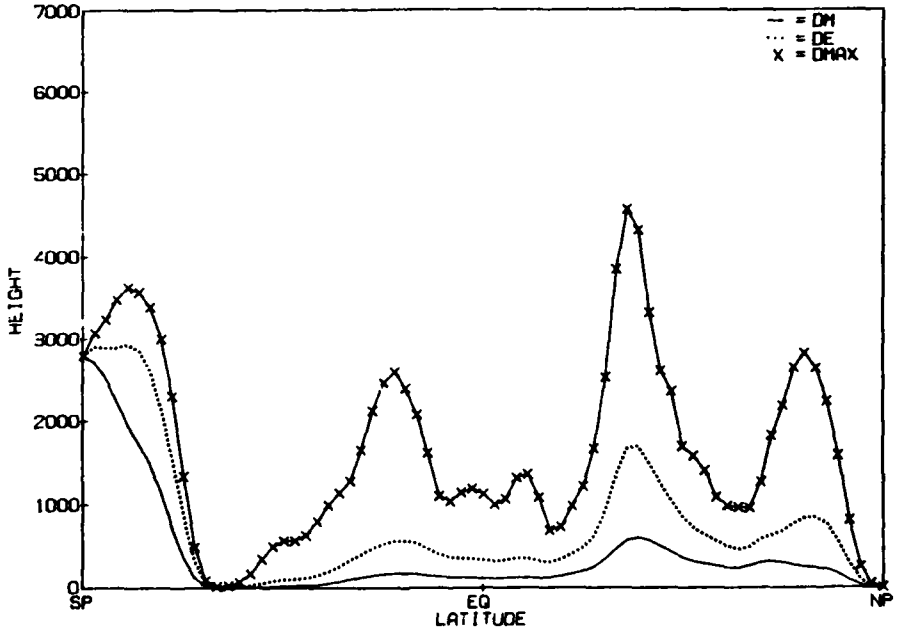

Figure 14b. Meridional Profiles of Terrain Parameters: DM-Zonal Mean, DE-Zonal Mean Plus Standard Deviation, DMAX-Maximum Value for Smoothed Terrain

by a solid curve, is the zonal mean; DE, represented by a dotted curve, is the sum of the zonal mean and the standard deviation of the field on the latitude; and DMAX, represented by a solid curve with crosses, is the maximum value of the field on the latitude.

Tables 8A and 8B tabulate the global rms of both the error in synthesis and the error in reproduction for both terrain fields at various truncations using either the trapezoidal or G-L quadratures with the 76 Gaussian latitudes. The 76 Gaussian latitudes form the smallest set required for the spectral model with the rhomboidal 30 truncation. The difference in characteristics between the error in synthesis, E_1, and the error in reproduction, E_2, is readily seen in the opposite trends of the variation of magnitude with truncation range. E decreases with widening of truncation range as more of the spectral components in the original fields are included. E_2, on the other hand, increases with widening of truncation range because of an increase in the number of polynomials whose degrees exceed the highest degree resolvable by the truncation.

Both tables support the preference of the G-L over the trapezoidal quadrature. Although the trapezoidal quadrature produces a slightly smaller rms error in synthesis, E_1, than the G-L quadrature for the unsmoothed terrain up to the rhomboidal 50 truncation, this small edge is more than compensated by disadvantages found in other aspects. For the smoothed terrain, the G-L quadrature produces a smaller E_1 for all truncations. More significantly, the rms error in reproduction increases more rapidly with the trapezoidal quadrature beyond the rhomboidal 40 truncation in the unsmoothed terrain and across the entire range in the smoothed terrain. It should also be noted that the global mean error is negligible in all cases.

Further support for favoring the G-L quadrature is provided by Table 9 which presents E_1' and E_2' (see Figure 13c for definition) for the two terrain fields. This table compiles the errors of transformation if the terrain fields had been available or defined on the Gaussian latitudes. The differences between the corresponding quantities in Tables 8a, 8b, and 9 represent the effect due to the extra step of interpolation from the 2.5° -interval latitudes to the Gaussian latitudes required in obtaining the measures E_1 and E_2 using the G-L quadrature. In terms of rms error in synthesis, this amounts to approximately $30 \sim 36$ m in the unsmoothed terrain and $3 \sim 5$ m in the smoothed terrain. The absence of the interpolation step in the calculation of E_2' brings forth the complete invertibility of the G-L quadrature as long as the truncation range does not exceed that specified by the number of Gaussian latitudes employed. The 76 Gaussian latitudes should reproduce exactly up to the rhomboidal 37 truncation, beyond which the error in reproduction should increase with further widening of truncation range. Table 9 bears witness to these theoretical inferences. In fact, the values of E_2' at

rhomboidal 60 and 70 truncations exceed those of E_2.

Table 8a. Root-Mean-Squares of the Error in Synthesis (E_1) and Error in Reproduction (E_2) With Different Rhomboidal Truncations of Unsmoothed Terrain (Units of m)

Error	Quadrature	Rhomboidal Truncation						
		15	24	30	40	50	60	70
E_1	T	272.44	206.32	175.08	137.79	103.20	88.66	96.49
	G-L	272.48	206.70	176.12	141.16	109.92	88.46	78.09
E_2	T	7.16	12.95	18.21	25.08	54.88	112.39	174.76
	G-L	6.96	14.64	19.92	26.19	32.03	38.96	50.88

Table 8b. Root-Mean-Squares of the Error in Synthesis (E_1) and Error in Reproduction (E_2) With Different Rhomboidal Truncations of Smoothed Terrain (Units of m)

Error	Quadrature	Rhomboidal Truncation						
		15	24	30	40	50	60	70
E_1	T	123.19	55.61	37.58	29.72	30.24	33.81	37.74
	G-L	123.14	55.14	35.88	24.46	19.46	16.58	14.81
E_2	T	7.10	12.54	17.05	24.83	35.06	47.17	57.39
	G-L	5.48	8.24	8.91	9.44	9.63	9.65	9.65

Comparisons of the rms of errors in Tables 8a, 8b, and 9 of the unsmoothed and smoothed terrain fields show the large contribution made by the smoothing operation in reducing both types of error, except in E_2' at truncation ranges where complete invertibility exists.

Tables 10A and 10B summarize the statistics of the errors in reproduction in the spectral domain, E_3 and E_3' for both terrain fields. Comparison with the corresponding quantities in the physical domain, shows the G-L quadrature produces smaller differences between the two domains than does the trapezoidal quadrature, while both quadratures exhibit similar characteristics in the variations of magnitude with truncation range as observed in E_2 and E_2'.

The spectral power of E_3 is found in seven subranges in each of the zonal and meridional spectra. The subranges are defined in terms of an integer K, which is one plus the zonal wave number, m, for the zonal spectrum and one plus the

Table 9. Root-Mean-Squares of the Error in Synthesis (E_1) and Error in Reproduction (E_2) With Different Rhomboidal Truncations With Reference to the Given Values on the Gaussian Latitudes of the Unsmoothed and Smoothed Terrain (Units of m).

Error	Field	Rhomboidal Truncation						
		15	24	30	40	50	60	70
E'_1	unsmoothed	238.98	170.96	140.18	106.16	77.36	58.34	50.21
	smoothed	117.61	51.25	32.33	20.80	15.42	12.01	9.68
E'_2	unsmoothed	R_2	R_2	R_2	9×10^{-5}	15.65	43.04	81.06
	smoothed	R_2	R_2	R_2	2×10^{-6}	0.19	0.83	1.79

$R_2 = 2 \times 10^{-7}$ is considered to be round-off error

difference, n - m, between the degree and order of a spherical harmonic component P_n^m for the meridional spectrum. The seven subranges are given in Table 11 [note that these subranges can be identified as horizontal or vertical lines, respectively, in Figure 2a as stated in Eqs. (20) and (21)]. Tables 12A and 12B summarize the power distributions for the trapezoidal quadrature and the G-L quadrature, respectively. The total powers are given in units of m^2 and the fractional powers in percent.

First, with the use of the trapezoidal quadrature, the spectral distributions of the error divide the truncation ranges considered into two groups, those with rhomboidal truncation lower than or higher than 40. All truncations up to rhomboidal 40 show the same spectral distributions in both the zonal and meridional spectra. The magnitudes of total power are approximately equal for the unsmoothed and smoothed terrains. All of the error in the zonal spectrum is contained in the zonal mean, while the error in the meridional spectrum increases towards the short-wave end. On the other hand, for truncations exceeding rhomboidal 40, a large error is found at the short-wave end of the zonal spectrum for the unsmoothed terrain. This error arises from the contributions of the short waves in the unsmoothed terrain that are effectively damped out by the smoothing operator. This is evident from the lack of any corresponding short-wave error in the smoothed terrain for which the error is all in the zonal mean. Also, the total power of the smoothed terrain is about the same as power of the zonal mean of the unsmoothed terrain. The distributions of the meridional spectra of the two terrain fields are similar, although the unsmoothed spectrum is more skewed towards the short-wave end.

Table 10a. The Square Roots of the Power of the Error in Reproduction in the Spectral Domain (E_3 or E_3') in the Unsmoothed Terrain (Unit = m)

Quadrature	Error	Rhomboidal Truncation						
		15	24	30	40	50	60	70
T	E_3	7.02	12.36	16.99	22.40	42.50	82.09	125.60
G-L	E_3	6.96	14.64	19.92	26.20	31.72	37.09	49.10
	E_3'	R_3	R_3	R_3	9×10^{-5}	11.30	30.77	57.61
$R_3 = 2 \times 10^{-7}$ is considered to be round-off error								

Table 10b. The Square Roots of the Power of the Error in Reproduction in the Spectral Domain (E_3 or E_3') in the Smoothed Terrain (Unit = m)

Quadrature	Error	Rhomboidal Truncation						
		15	24	30	40	50	60	70
T	E_3	6.96	11.97	15.91	22.18	29.87	38.45	45.64
G-L	E_3	5.48	8.24	8.91	9.44	9.63	9.68	9.75
	E_3'	R_3	R_3	R_3	2×10^{-6}	0.19	0.87	1.74
$R_3 = 2 \times 10^{-7}$ is considered to be round-off error								

Unlike the trapezoidal quadrature, the G-L quadrature exhibits considerable differences in both the total magnitudes and the spectral distributions of the error for the two terrains for all truncation ranges. For the unsmoothed terrain with truncations less than 40, the G-L quadrature produces errors that are larger than the trapezoidal quadrature. For truncations beyond rhomboidal 40, the G-L errors are significantly less than the trapezoidal errors. For the smoothed terrain, however, the G-L quadrature produces errors that are much less than those of the trapezoidal quadrature. These errors also increase much more slowly with the widening of truncation range than all others. The spectral distributions tend to be mound-shaped for the smoothed terrain for both the zonal and meridional spectra. For the unsmoothed terrain, the distributions are skewed towards the short-wave end.

The influence of the differences in the terrain fields on model performance was assessed in terms of the global rms errors of the height forecasts of the

Table 11. Definition of Spectral Ranges Used in Tables 12a and 12b. Given are the lower and upper bounds for each index, K

Index (K)	Lower	Upper
1	0	0
2	1	3
3	4	9
4	10	15
5	16	24
6	25	30
7	31	M

Table 12a. Total Power (in m^2) and Spectral Composition (in Percent) of E_3 for Trapezoidal Quadrature (L = Zonal, M = Meridional)

		Rhomboidal Truncation													
		15		24		30		40		50		60		70	
		U	S	U	S	U	S	U	S	U	S	U	S	U	S
Total Power		49	48	153	143	289	253	502	492	1806	892	6738	1479	15775	2083
1	L	100	100	100	100	100	100	100	100	47	100	21	100	13	100
	M	0	0	0	0	0	0	0	0	0	0	0	0	0	0
2	L	0	0	0	0	0	0	0	0	0	0	0	0	0	0
	M	6	6	2	2	2	2	1	1	0	0	0	0	0	0
3	L	0	0	0	0	0	0	0	0	0	0	0	0	2	0
	M	34	32	13	13	9	9	5	5	2	3	1	3	1	2
4	L	0	0	0	0	0	0	0	0	0	0	0	0	5	0
	M	62	62	25	25	17	17	10	10	3	6	1	5	4	4
5	L	0	0	0	0	0	0	0	0	0	0	9	0	11	0
	M	0	0	59	59	39	39	23	23	7	15	6	11	8	10
6	L	0	0	0	0	0	0	0	0	7		11		12	0
	M	0	0	0	0	34	34	20	20	7	13	6	10	6	8
7	L	0	0	0	0	0	0	0	0	51	0	58	0	57	0
	M	0	0	0	0	0	0	42	42	81	61	85	71	81	75

Table 12b. Total Power (in m^2) and Spectral Composition (in Percent) of E_3 for Gauss-Legendre Quadrature (L = Zonal, M = Meridional)

		Rhomboidal Truncation													
		15		24		30		40		50		60		70	
		U	S	U	S	U	S	U	S	U	S	U	S	U	S
Total	Power	48	30	214	68	397	79	686	89	1911	93	1376	94	2411	95
1	L	8	11	4	71	3	8	3	7	3	8	3	8	2	7
	M	0	0	0	0	0	0	0	0	0	0	0	0	0	0
2	L	38	46	24	42	17	40	16	38	14	39	13	39	8	38
	M	6	8	2	4	1	4	1	3	0	3	0	3	0	3
3	L	26	26	23	28	16	27	17	28	18	28	16	28	10	28
	M	27	32	9	18	6	16	4	14	3	14	3	14	6	13
4	L	28	18	19	14	16	14	15	15	14	14	12	14	8	15
	M	67	60	23	29	15	26	10	23	8	23	7	22	11	22
5	L	0	0	31	8	29	8	23	9	19	8	16	9	12	9
	M	0	0	66	48	44	39	30	35	22	34	19	34	16	33
6	L	0	0	0	0	19	2	15	2	13	2	11	2	9	2
	M	0	0	0	0	33	15	22	12	16	11	14	12	11	11
7	L	0	0	0	0	0	0	12	0	19	1	30	0	52	1
	M	0	0	0	0	0	0	33	11	50	15	57	16	56	17

mandatory pressure levels. For this purpose, a comparison was made among six 72-hour forecasts, three forecasts with each terrain field (unsmoothed and smoothed) beginning from 00Z on 15, 16, and 17 January 1978. The results are summarized in Figures 15 and 16.

Figure 15 shows the vertical profile of the group means of the global rms of (1) the processing error at the initial time, and (2) the forecast errors at days one, two, and three. It is quite obvious that little difference exists in both the magnitudes and shapes of the profiles as a result of differences in the terrain fields. It is also clear that the processing error constitutes a small fraction of the forecast errors. No discernible difference exists in the forecast errors that could be ascribed to the difference in processing errors at the initial time.

To probe further into the relationship between the initial processing errors and the forecast errors, the group means and standard deviations of the

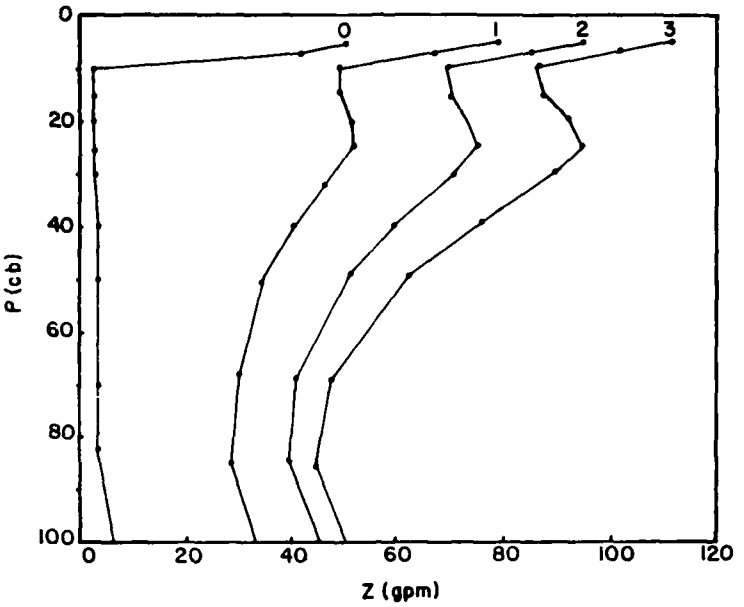

Figure 15a. Vertical Profiles of the Group Means of the Global RMS of the Processing Error at Day 0 and the Forecast Errors at Days 1, 2, and 3: Unsmoothed Topography

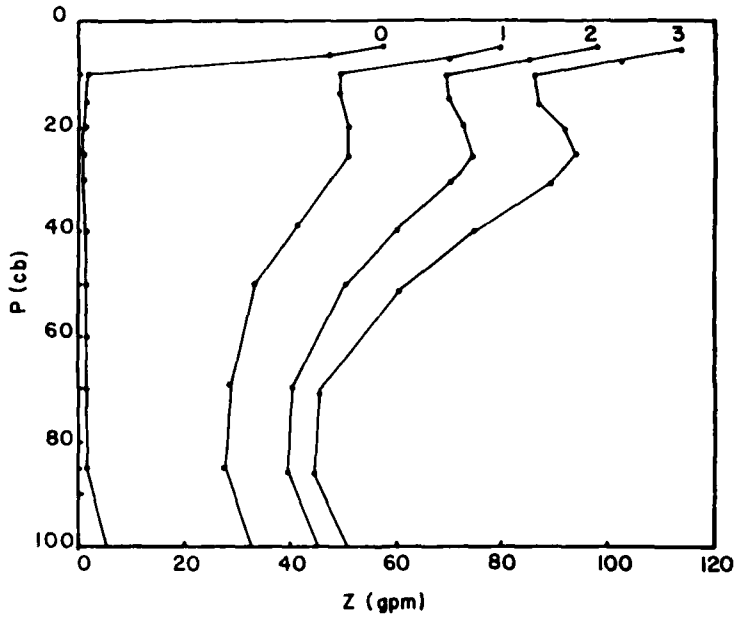

Figure 15b. Vertical Profiles of the Group Means of the Global RMS of the Processing Error at Day 0 and the Forecast Errors at Days 1, 2, and 3: Smoothed Topography

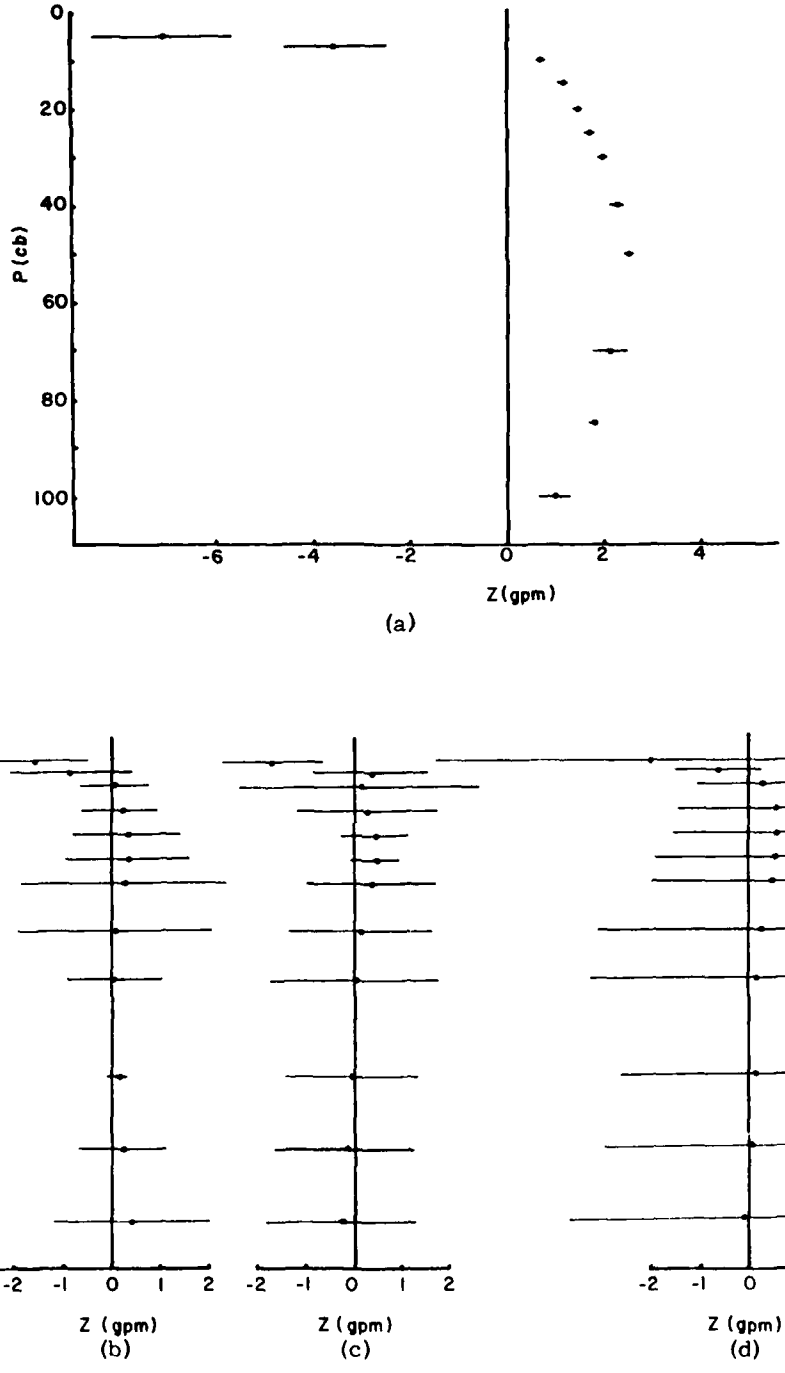

Figure 16. Vertical Profiles of the Group Means and Standard Deviations of the Differences Between the Global RMS Errors Using Different Terrain Fields: (a) Processing Error at Day 0, and Forecast Errors at (b) Day 1, (c) Day 2, and (d) Day 3

differences between the global rms errors for forecasts with the two terrain fields were calculated. The results are shown in Figure 16, where a dot represents the group mean and the width of the line across the dot represents twice the group standard deviation. Here, a positive value indicates a smaller error with the smoothed topography and vice versa. From Figure 16A, it is apparent that use of the smoothed terrain reduced the processing error at all levels except the top two (50 mb and 70 mb). However, no significant trace of this improvement appeared in the forecasts. The differences in the forecast errors (Figures 16b, 16c, and 16d) were smaller than the differences in the processing errors and were much smaller than the forecast errors themselves. Furthermore, these differences were not statistically significant.

On the basis of these findings, it can be concluded that, in using a spectral model for simulating and predicting the global circulation; (1) the terrain is best defined on the Gaussian latitudes of the forecast model; (2) the Gauss-Legendre quadrature is better than the trapezoidal quadrature in the computation of the transforms; and (3) the smoothed terrain is preferable as the model terrain. Thus, the terrain to be used in the high-resolution model is defined as the set of the spherical harmonic coefficients obtained from the original FGGE data by first passing them through the 9-point smoother twice, interpolating the results linearly in $\sin\phi$ to the 76 Gaussian latitudes, and then transforming them into spectral coefficients at the rhomboidal 30 truncation. The model terrain is thereby uniquely defined in both the physical and spectral domains. For consistency, this terrain field is also used in the preprocessing and postprocessing steps.

8. EFFECTS OF INITIALIZATION

"Initialization" is the term generally used for the procedure through which unwanted meteorological noise is suppressed. This noise usually appears as spurious gravity waves that, if left unchecked, could contaminate and possibly destroy the forecast. These waves are generated by certain imbalances between the mass and motion fields. There are three possible sources for these imbalances: (1) errors in the observations, (2) errors in the analysis scheme interpolating observations to grid points, and (3) the forecast model itself, since it is a discrete representation of a continuous fluid. While there is general agreement within the numerical weather prediction community on the need for initialization, it is not clear what form initialization should take or to what extent it is necessary.

To assess the impact of initialization on the model, several high-resolution (30**R**12) forecasts using different initialization techniques have been run and com-

pared. The methods that were tested fall into two broad categories: (1) those in which the initial data are filtered and balanced (for example, normal mode methods) and (2) those where the spurious waves are controlled during the forecast by the numerics and/or the parameterized physics of the model. Specifically, three different methods were tested: (1) no initialization at all, (2) linear damping of divergence as described by Bourke[9] and referred to as "divergence dissipation," and (3) the Machenhauer[10] nonlinear normal mode initialization process. All three methods were tested on forecasts run from data produced by two different analysis schemes, the 1978 FGGE III-A Hough analysis[11] (denoted as HO) and the 1979 FGGE III-A optimal interpolation (OI) analysis.[12] It should be noted that the Hough analysis implicitly includes linear normal mode initialization since the amplitudes of the gravity modes are set to zero by the analysis scheme. In view of this, it was felt that Hough based forecasts alone were not sufficient to properly assess the effects of initialization, and thus OI based forecasts were also run. The forecasts that were run for the six different combinations of analysis and initialization and their acronyms are summarized in Table 13.

Table 13. Summary and Acronyms of Different Combinations of Analysis and Initialization That Were Tested

Initialization Method	Analysis Scheme	
	Hough (HO)	Optimal Interpolation (OI)
No initialization (NO)	HO-NO	OI-NO
Divergence dissipation (DD)	HO-DD	OI-DD
Nonlinear normal mode (NM)	HO-NM	OI-NM

9. Bourke, W. (1974) A multi-level spectral model. I. Formulation and hemispheric integrations, Mon. Wea. Rev. 102:687-701.

10. Machenhauer, B. (1977) On the dynamics of gravity oscillations in a shallow water model with applications to normal mode initialization, Beit. Phys. Atmos. 50:253-271

11. Flattery, T. (1971) Spectral models for global analysis and forecasting, Proc. Sixth AWS Tech. Exchange Conf., U.S. Naval Academy, Annapolis, Md., 21-24 September 1970, AWS-TR-242:42-54.

12. McPherson, R.D., Bergman, K.H., Kistler, R.E., Rasch, G.E., and Gordon, D.S. (1979) The NMC operational global data assimilation system, Mon. Wea. Rev. 107:1445-1461.

In the no-initialization cases (NO), no initialization procedure is used (except implicitly in the Hough analysis as noted above). The gravity waves are controlled in the forecast model by the semi-implicit time scheme that is known to damp gravity waves.[13] A certain amount of dissipation is also provided by the parameterized subgrid scale diffusion, which is a linear horizontal ∇^4 operator applied to vorticity, divergence, temperature, and specific humidity. The values of the diffusion coefficients are 5×10^{16} m^4 s^{-1} for divergence (applied to all spectral components) and 1×10^{16} m^4 s^{-1} for the other variables (applied only to the upper half of the rhomboid, $n > M$).

For divergence dissipation (DD), the initial values of all spectral components of divergence are set to zero. The subgrid scale diffusion of divergence is replaced by a linear damping term of the form -KD where the damping coefficient, K, is given by

$$K = \begin{cases} 5 \times 10^{-4} \exp(-0.19188\ t)\ s^{-1} & t \leq 24\ h \\ 5 \times 10^{-6}\ s^{-1} & t > 24\ h \end{cases} \quad (37)$$

where t is given in hours.

Diffusion is applied to vorticity, temperature, and specific humidity as described above.

For the nonlinear normal mode initialization cases (NM), the analyzed data are filtered and balanced according to Machenhauer's[10] scheme. In this procedure, the data are projected onto the normal modes of the model and separated into the rotational or Rossby modes and the gravity modes. The gravity modes are adjusted in such a way that the linear tendency terms are balanced by the adiabatic nonlinear advective terms, thus resulting in a net initial gravity wave tendency of zero. The procedure consists of two iterations applied only to the first four vertical modes. Further details of the scheme are given by Ballish.[14] In the NM forecasts, subgrid scale diffusion is included as in the NO cases.

To assess the impact of initialization on the forecasts, the discussion will focus on the changes in time of the divergence field because it is the quantity that is most dramatically affected by initialization. In terms of the effect of nonlinear normal mode initialization on the analyzed data, the results were as expected: very little change in the Hough data but substantial change in the OI

13. Kurihara, Y. (1965) On the use of implicit and iterative methods for the time integration of the wave equation, Mon. Wea. Rev. 93:33-46.

14. Ballish, A.B. (1980) Initialization Theory and Application to the NMC Spectral Model, Ph.D. thesis, U. of Maryland.

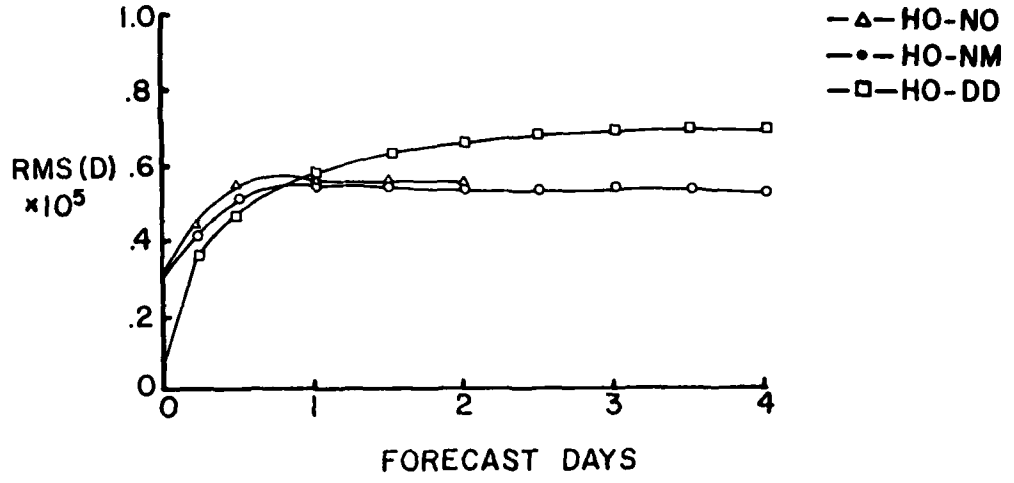

Figure 17. Growth Rate of Vertically Integrated Global RMS Divergence for High-Resolution Forecasts Using Different Methods of Initialization, Beginning From 00Z 17 January 1978 (FGGE III-A, Hough Analysis)

data (see Figures 18a and 20a). The typical rms 500 mb height changes resulting from nonlinear normal mode initialization were 12 m for the Hough analysis and 25 m for the OI, while the typical rms changes in the average 1000-200 mb heights were 15 m and 28 m respectively. Figure 17 shows an example of the vertically integrated global rms divergence computed from spectral coefficients at the model σ -layers as a function of forecast time for the HO-NO, HO-DD, and HO-NM forecasts beginning from the Hough analysis of 00Z 17 January 1978. The OI example is shown in Figure 19 for forecasts beginning from 12Z 17 February 1979.

Returning to Figure 17, it can be seen that the Hough analysis is practically nondivergent. The forecast model generates its own divergence field with a spin-up time of roughly 36 hours. The HO-NO and HO-NM runs are quite close while the HO-DD forecast develops a somewhat larger divergence field after 24 hours. This is caused by the difference in the form of divergence damping between the NO, NM runs and the DD run. In the NO, NM cases, the divergence is subjected to a highly scale-selective ∇^4 diffusion with e-folding times ranging from 261 years for the largest scales (n = 1) to 41 minutes for the smallest resolved scales (n = 60). For DD, the damping term is independent of scale, with an e-folding time of 55 hours (for forecast times beyond 24 hours). The net result is that the larger scales (for $n < 20$) are more strongly damped by DD, while the smaller scales ($n \geq 20$) are more strongly damped by the ∇^4 diffusion operator. Thus, the larger value of divergence after day one in the HO-DD forecast results from the increased short-wave activity. Figure 18 shows the vertical profiles of the global rms

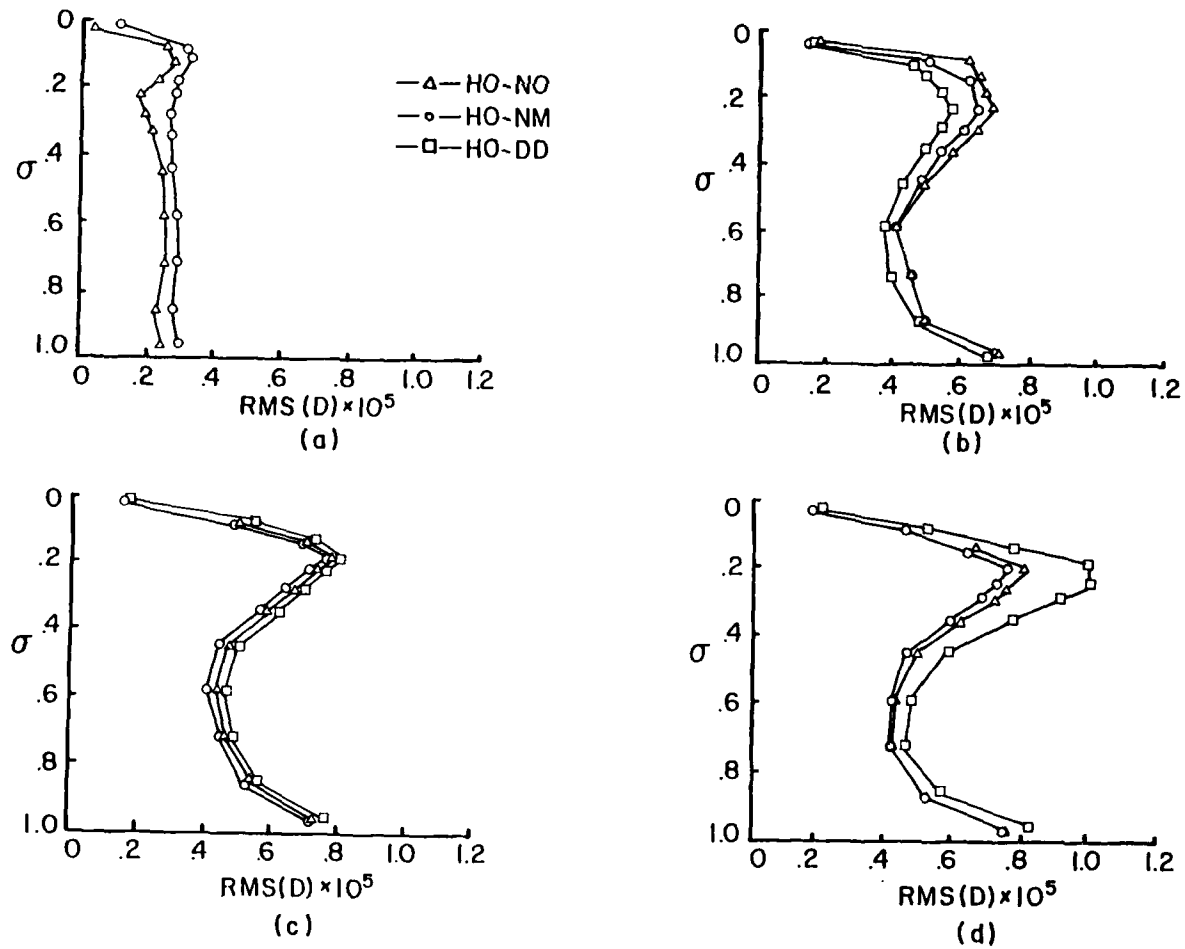

Figure 18. Vertical Profiles (Model σ-Layers) of RMS Divergence for High-Resolution Forecasts Using Different Methods of Initialization Beginning From 00Z 17 January 1978: (a) Initial Values, (b) 12 Hours, (c) 24 Hours, and (d) 48 Hours

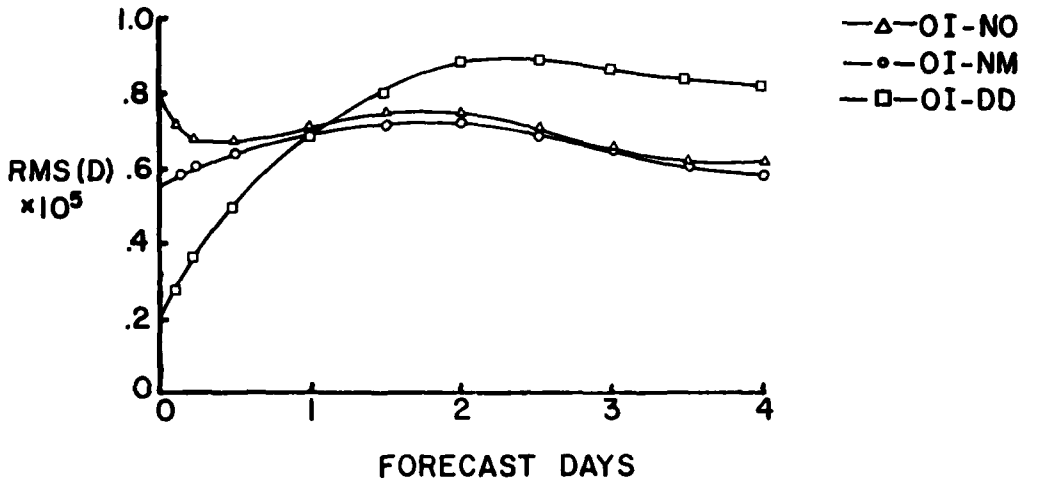

Figure 19. Growth Rate of Vertically Integrated Global RMS Divergence for High-Resolution Forecasts Using Different Methods of Initialization, Beginning From 12Z 17 February 1979 (FGGE III-A, Optimal Interpolation)

divergence for the forecasts (at the model σ-layers) at (a) the initial time, (b) 12 hours, (c) 24 hours, and (d) 48 hours. An interesting feature of the initial data is that the nonlinear normal mode initialization procedure modestly increases the divergence in contrast to the large decrease found in the OI data after the initialization procedure is applied (see Figures 20a and 21 and discussion below). Throughout the 48-hour period, the HO-NO and HO-NM profiles are quite close to one another. The divergence spin-up is most noticeable in the HO-DD profiles, which exceed the others at 24 and 48 hours for reasons discussed above.

In view of the small differences between the HO-NO and HO-NM forecasts, it was decided to carry out similar tests with 1979 FGGE III-A data which was produced by an OI scheme.[12] This analysis scheme does not contain any implicit linear normal mode initialization. Thus, it was felt that these results would provide a better measure of the impact of initialization. Figure 19 shows the vertically integrated global rms divergence as a function of forecast time for the OI-NO, OI-NM, and OI-DD forecasts starting from 12Z 17 February 1979. In contrast to the Hough case, it can immediately be seen that the OI analyzed divergence is much larger and that the nonlinear normal mode initialization procedure reduces the global value by more than 40 percent. This is also quite apparent in Figure 20a. Another interesting feature here is that the OI-NM forecast spins up slightly from the initial value of divergence, while in the OI-NO forecast, the model damps the unusually large initial value. As in the Hough case, the OI-NO and OI-NM runs are quite close, while the OI-DD run produces a larger diver-

gence field beyond day one.

Figure 20 shows the vertical profiles of the global rms divergence (at the model σ-layers) for the OI example for (a) the initial time, (b) 2 hours, (c) 6 hours, (d) 12 hours, (e) 24 hours, (f) 48 hours, and (g) 72 hours. The most striking feature here is the extremely large value in the top model layer and the change in both the magnitude and shape of the profile after the nonlinear normal mode initialization is applied. To be sure that this was not due to a data error in this particular data set and/or a problem with the vertical interpolation in the preprocessor, the global rms divergence was computed directly on the mandatory pressure levels for 12Z 18 February 1979. This profile is labelled NO in Figure 21a. Once again, the extremely large divergence value at 50 mb can be seen. The NM profile in this figure is the result of the postprocessing (on to the mandatory pressure levels) of the initialized spectral coefficients. Figure 19b shows the vertical profiles of the model σ-layers and appears quite similar to Figure 20a. Similar profiles were also found in January 1979 data.

Returning to Figures 20b - 20g it can be seen that the largest differences between the OI-NO and OI-NM profiles occur prior to 24 hours. Clearly, beyond 24 hours, the combined effects of the semi-implicit time scheme and the subgrid scale diffusion are sufficient to control the spurious gravity waves even in the no-initialization case. As in the Hough case, the OI-DD forecast here also produces values of divergence that are larger than those in the OI-NO and OI-NM forecasts.

Finally, Figure 22 shows northern hemisphere plots of the differences between the OI-NM and OI-NO velocity potential at $\sigma = .5$ at (a) 6 hours, and (b) 48 hours for the forecasts from 12Z 17 February 1979. As might be expected, the 6-hour field shows quite a bit of activity, while the 48-hour field reflects the small difference between the OI-NM and OI-NO forecasts at this time. The corresponding 500 mb rms height differences between the two forecasts are 9 m and 6 m at 6 hours and 48 hours respectively. Based on these sample forecasts, it is seen that the major impact of initialization is found in the very short range (less than 24 hours) forecasts. The main role of these short range forecasts (6-12 hours) is to provide a first-guess field for the analysis/data assimilation cycle. As such, the nonlinear normal initialization procedure should be viewed as part of and necessary for the analysis scheme. While it may help the forecast, it does not seem to play a crucial role in shaping the forecasts in the range of 24-96 hours.

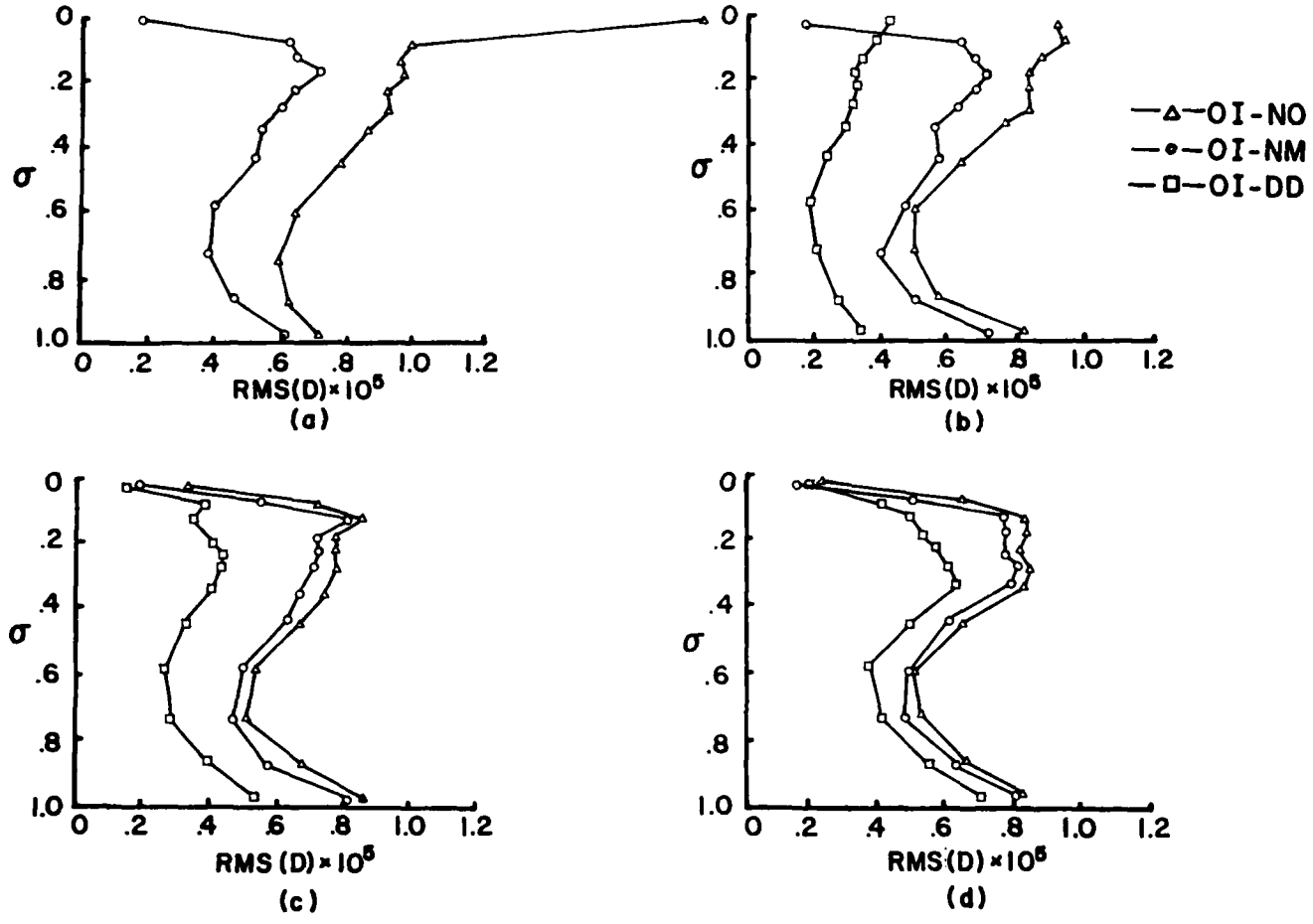

Figure 20. Vertical Profiles (Model σ-Layers) of RMS Divergence for High-Resolution Forecasts Using Different Methods of Initialization: (a) Initial Values, and Forecast Errors Beginning From 12Z 17 February 1979, (b) 2 Hours, (c) 6 Hours, (d) 12 Hours

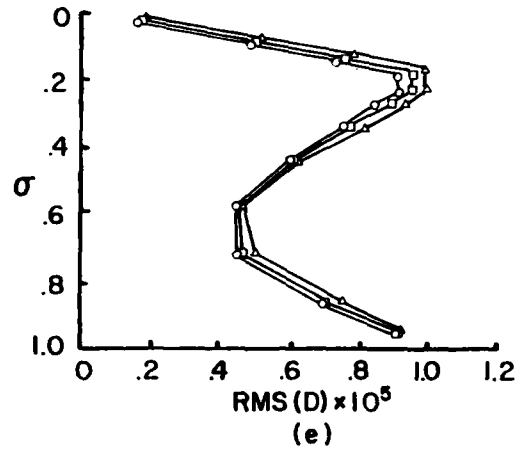

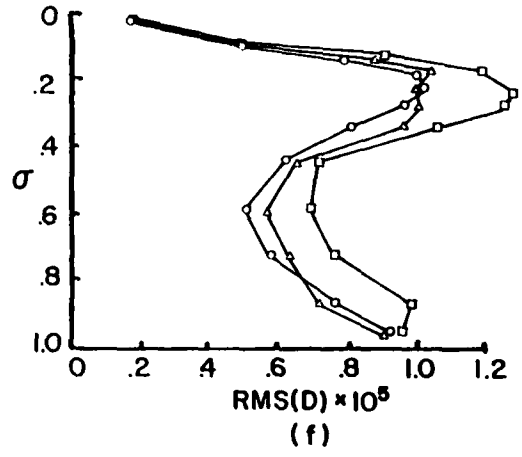

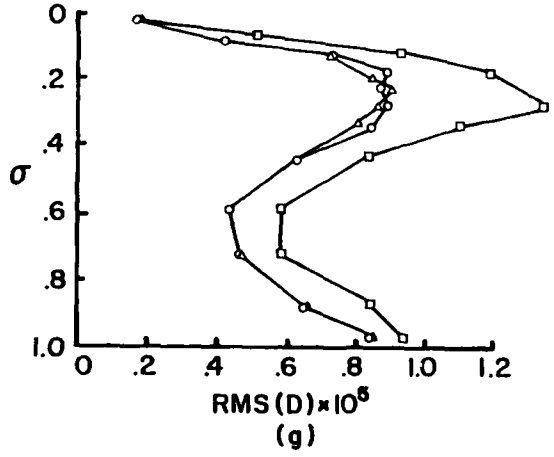

Figure 20 (Contd). Vertical Profiles (Model σ-Layers) of RMS Divergence for High-Resolution Forecasts Using Different Methods of Initialization: (a) Initial Values, and Forecast Errors Beginning From 12Z 17 February 1979, (b) 2 Hours, (c) 6 Hours, (d) 12 Hours

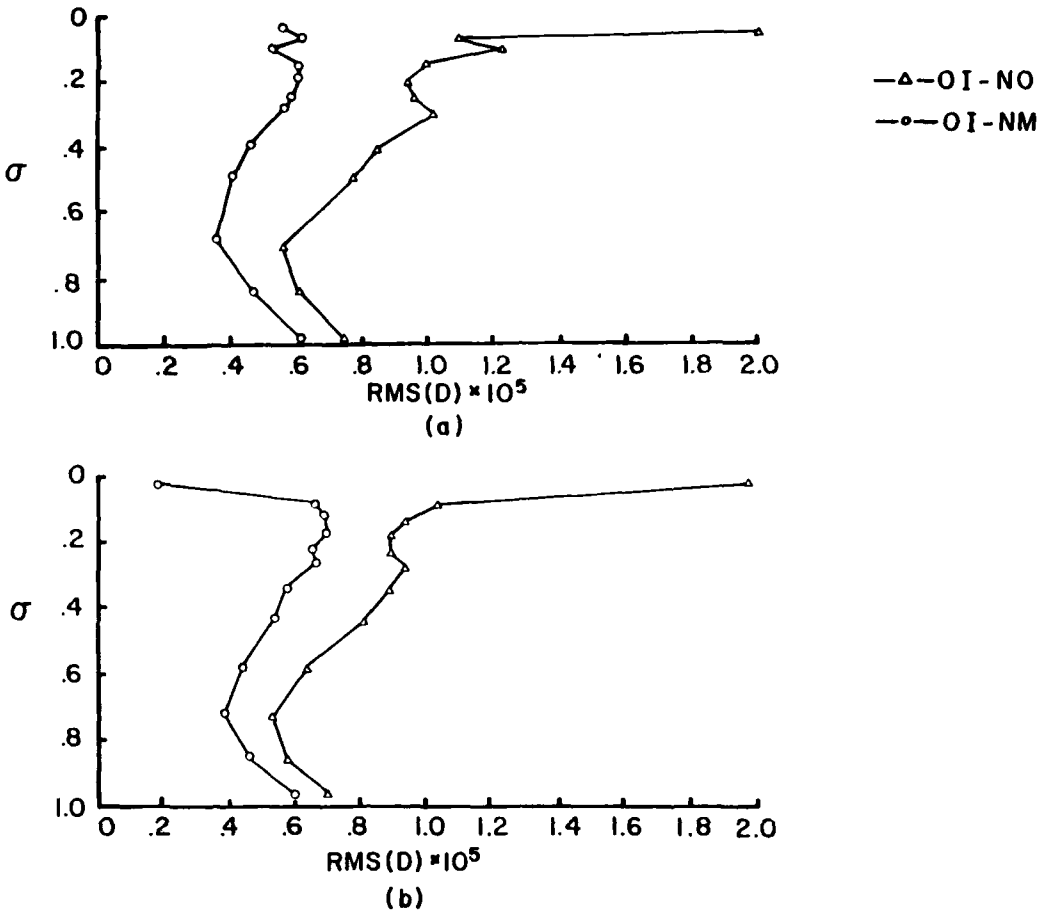

Figure 21. Vertical Profiles of RMS Divergence for High-Resolution Data on 12Z 18 February 1979: (a) Mandatory Pressure Levels, and (b) Model σ Layers

9. CONCLUSION

The flexible resolution/truncation version of the AFGL global spectral model as adapted to the CRAY-1 has been described. The numerical formulation and physical parameterizations are the same as in the baseline model described by Brenner et al.[1] Significant restructuring of the code was necessary for efficient use of the CRAY's vector-processing capabilities. This resulted in a substantial reduction of execution time for the forecast model.

To test the performance of the model, a series of low-resolution (15R6) and high-resolution (30R12) forecasts have been run and compared. The 12 layers of the high-resolution model are the same as in the NMC operational model. The

initial and verifying data consisted of FGGE III-A analyses (Hough) from January and July 1978. In general, increasing the resolution resulted in reduced forecast errors in the 24-96-hour range. By 96 hours, the low-resolution model loses its skill in forecasting the height fields. The high-resolution forecasts are still useful at 96 hours and probably retain some skill for forecasts up to six or seven days. The major weakness is in the humidity forecasts, which show very minimal skill. This characteristic seems to be rather insensitive to increases in resolution. This is caused partly by the poor quality of the humidity fields produced by the Hough analysis. Other possible sources of this problem are the moisture physics schemes and the vertical advection scheme as applied to specific humidity. Both of these possibilities are currently being studied.

Two other topics studied with the high-resolution model were the representation of topography and the effects of initialization. In the former, we found that the most appropriate terrain field for the forecast model is the so-called smoothed topography. It is produced by taking the gridded (2.5° x 2.5°) topography, passing it through a nine-point smoother twice, interpolating to the model's Gaussian grid, and spectrally truncating at the model's resolution. The reasons for this choice are to provide consistency between the pre- and postprocessing procedures and to have a uniquely defined and reproducible terrain field.

In assessing the impact of initialization, it was found that beyond 24 hours, the forecast is not greatly affected by filtering or initialization of the initial data. The damping characteristics of the semi-implicit time scheme and subgrid scale diffusion can control any undesirable gravity waves. The effects of the normal mode initialization procedure are felt mostly in the very short range (less than 24 hours) forecasts, and it is therefore needed primarily to provide smooth first-guess fields (6- or 12-hour forecasts) for the analysis/data assimilation cycle.

Finally, the future research efforts in global modeling will be directed towards improving the accuracy and efficiency of the forecasts with special emphasis on improving the humidity forecasts and implementing cloud forecasting routines. Much of the work over the next two years will be incorporating and testing the newly developed physical parameterization packages, which include boundary layer, cumulus parameterization, and radiation schemes. In addition, more efficient transform routines will be incorporated as well as alternative numerical treatment of the moisture equation. A more accurate humidity analysis scheme will also be completed within the next year.

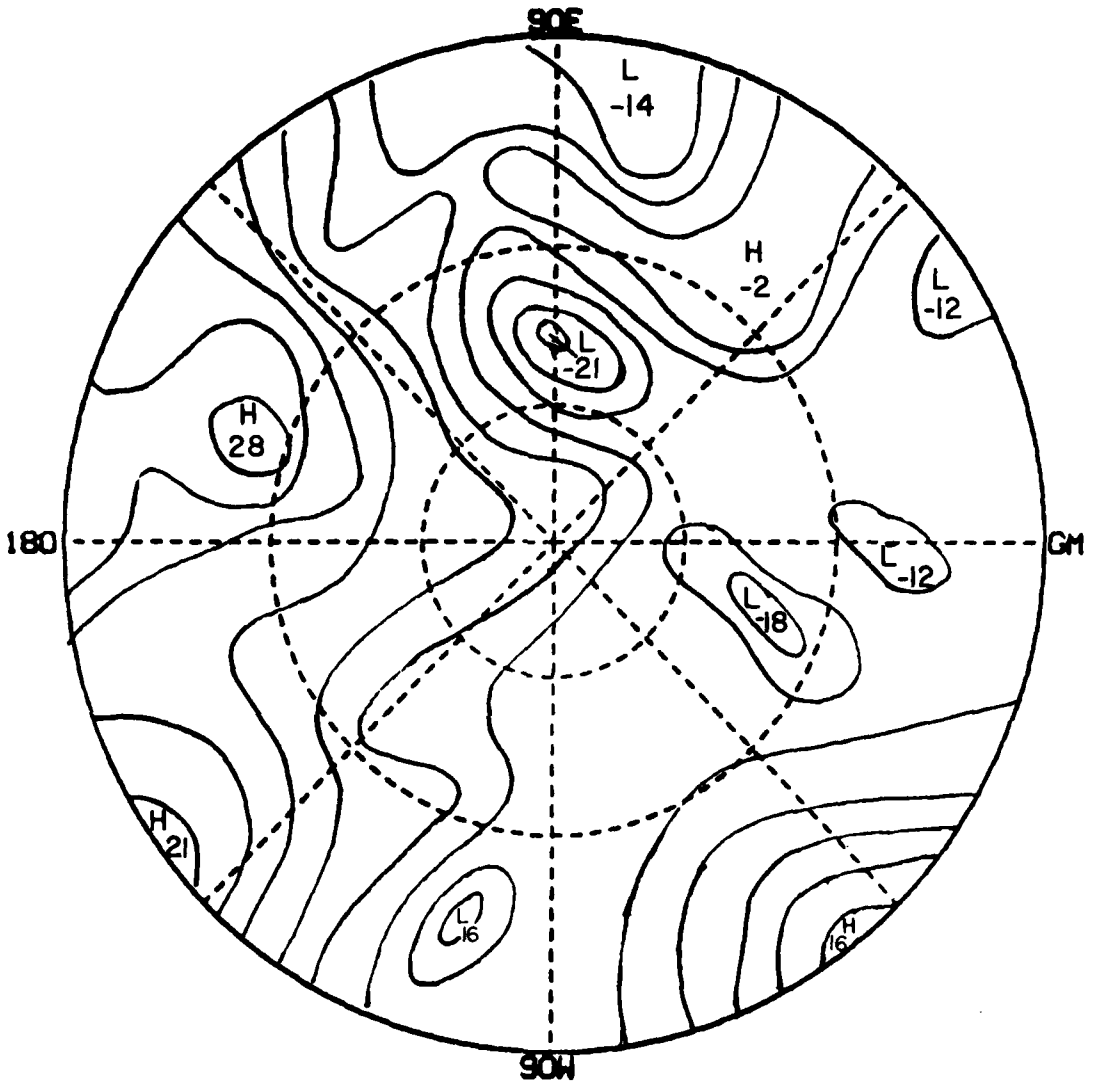

Figure 22a. Difference Between Initialized and Uninitialized Velocity Potential at $\sigma = .5$ for Forecasts Beginning From 12Z 17 February 1979: 6-Hour Forecast. Contour interval is 5 x 10^5 $m^2 s^{-1}$

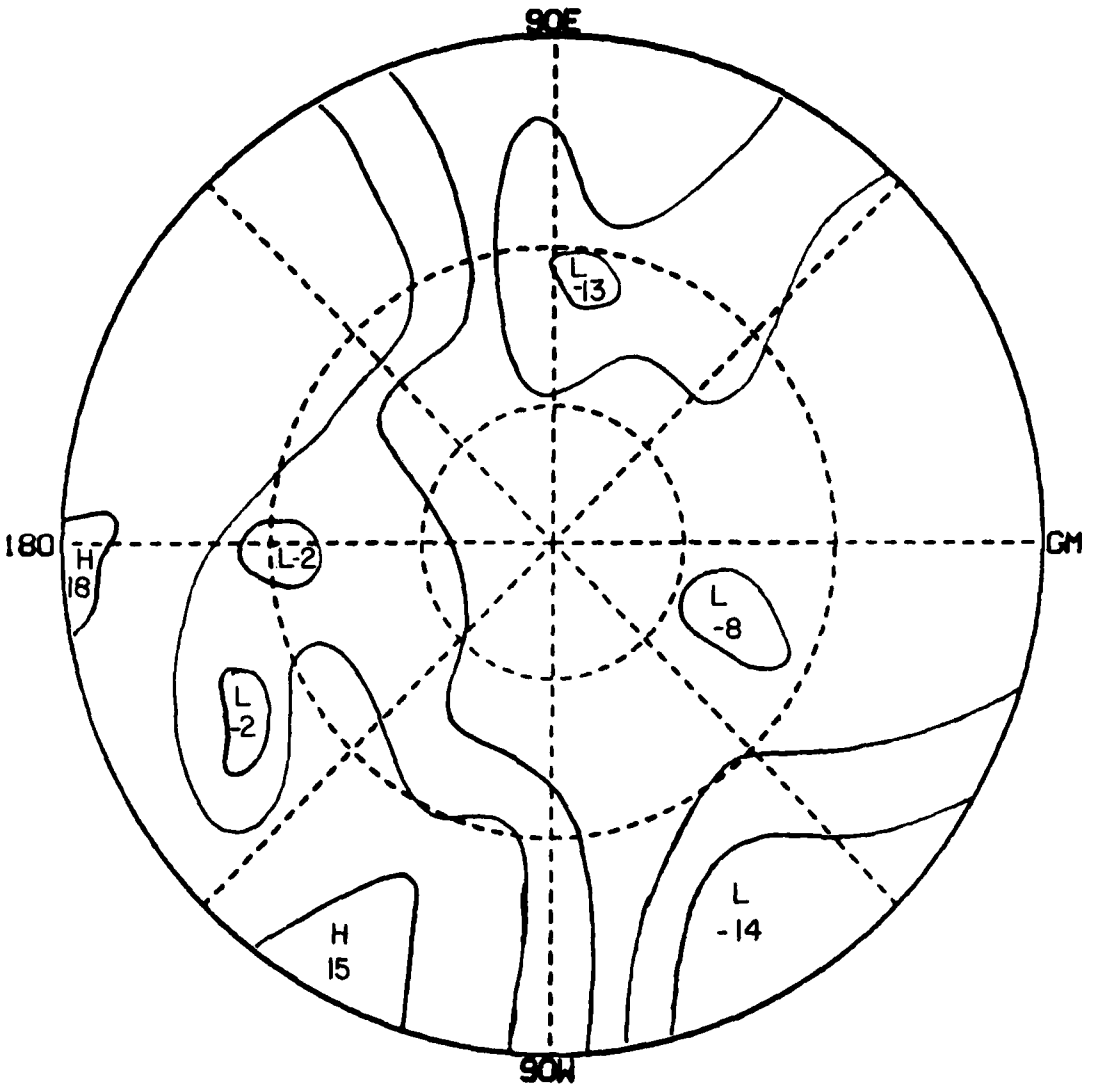

Figure 22b. Difference Between Initialized and Unitialized Velocity Potential at $\sigma = .5$ for Forecasts Beginning From 12Z 17 February 1979: 48-Hour Forecast. Contour interval is 5 x 10^5 $m^2 s^{-1}$

References

1. Brenner, S., Yang, C., and Yee, S. (1982) The AFGL Spectral Model of the Moist Global Atmosphere: Documentation of the Baseline Version, AFGL-TR-82-0393, AD A129283.

2. Eliasen, E., Machenauer, B., and Rasmussen, E. (1970) On a Numerical Method for Integration of the Hydrodynamical Equations With a Spectral Representation of the Horizontal Fields, Inst. of Theoret. Meteor., U. of Copenhagen, Report No. 2.

3. Orszag, S.A. (1970) Transform method for calculation of vector coupled sums: Application to the spectral form of the vorticity equation, J. Atmos. Sci. 27:890-895.

4. Sela, J. (1980) Spectral modeling at the National Meteorological Center, Mon. Wea. Rev. 108:1279-1292.

5. Mitchell, K., and Yang, C. (1985) A Comparison of Moisture Variables in the Vertical Interpolation of a 4-D Data Assimilation System, AFGL-TR-85-0090.

6. Bengstsson, L. (1981) Numerical prediction of atmospheric blocking: A case study, Tellus 33:19-42.

7. Sirutis, J., Miyakoda, K., and Ploshay, J. (1980) Moisture distribution dereived in mathematical models and four dimensional assimilation, in Atmospheric Water Vapor, Academic Press, New York, pp. 489-496.

8. Nieminen, R. (1983) Operational Verification of ECMWF Forecast Fields and Results for 1980-1981, ECMWF Technical Report No. 36.

9. Bourke, W. (1974) A multi-level spectral model. I. Formulation and hemispheric integrations, Mon. Wea. Rev. 102:687-701.

10. Machenhauer, B. (1977) On the dynamics of gravity oscillations in a shallow water model with applications to normal mode initialization, Beit. Phys. Atmos. 50:253-271.

11. Flattery, T. (1971) Spectral models for global analysis and forecasting, Proc. Sixth AWS Tech. Exchange Conf., U.S. Naval Academy, Annapolis, Md., 21-24 September 1970, AWS-TR-242:42-54.

12. McPherson, R.D., Bergman, K.H., Kistler, R.E., Rasch, G.E., and Gordon, D.S. (1979) The NMC operational global data assimilation system, Mon. Wea. Rev. 107:1445-1461.

13. Kurihara, Y. (1965) On the use of implicit and iterative methods for the time integration of the wave equation, Mon. Wea. Rev. 93:33-46.

14. Ballish, A.B. (1980) Initialization Theory and Application to the NMC Spectral Model, Ph.D. thesis, U. of Maryland.

List of Symbols

a	radius of the earth
g	gravity
i	$\sqrt{-1}$
j, k, l	indices
$\underset{\sim}{k}$	vertical unit vector
m	order of spherical harmonic (*superscript*)
n	degree of spherical harmonic (subscript)
p	pressure
p_*	surface pressure
q	$\ln p_*$
t	time
u, v	eastward and northward components of velocity
A, B	nonlinear advection terms
C_p	specific heat at constant pressure
D	horizontal divergence
H	diabatic heating
H_n^m	meridional derivative of the associated Legendre function
K	number of vertical layers
M	truncation value of m
N	truncation value of n
P_n^m	associated Legendre function of order m and degree n
Q	specific humidity
R	gas constant for dry air

T	temperature
T_0	basic state temperature
U, V	pseudo-velocity = $u \cos\phi$, $v \cos\phi$
W_j	Gaussian weight
ζ	relative vorticity
η	absolute vorticity
θ	potential temperature
κ	R/C_p
λ	longitude
μ	sin
ν	diffusion coefficient
σ	vertical coordinate
$\dot{\sigma}$	vertical velocity = $\frac{d\sigma}{dt}$
ϕ	latitude
χ	velocity potential
ψ	streamfunction
Φ	geopotential
Φ_*	surface geopotential
Ω	angular velocity of the earth's rotation
$( )_n^m$	spherical harmonic coefficient of order m and degree n
$\overline{( )}$	vertical integral
$( )_k$	layer value
$\tilde{( )}_k$	level (interface) value
$\underset{\sim}{( )}$	vector

END

FILMED

11-85

DTIC